Synergistic Coding of Human Odorants in the Mosquito Brain

Shruti Shankar [1], Genevieve M. Tauxe [1], Emma D. Spikol [2], Ming Li [3], Omar S. Akbari [3], Diego Giraldo [1], Conor J. McMeniman [1, 2, *]

[1] W. Harry Feinstone Department of Molecular Microbiology and Immunology, Johns Hopkins Malaria Research Institute, Johns Hopkins Bloomberg School of Public Health, Johns Hopkins University, Baltimore, MD 21205, USA.

[2] The Solomon H. Snyder Department of Neuroscience, Johns Hopkins University School of Medicine, Baltimore, MD 21205, USA.

[3] Section of Cell and Developmental Biology, University of California, San Diego, La Jolla, CA, 92093, USA.

*Corresponding author
Email: cmcmeni1@jhu.edu

Abstract:

The yellow fever mosquito *Aedes aegypti* employs olfaction to locate humans. We applied CRISPR-Cas9 genome engineering and neural activity mapping to define the molecular and cellular logic of how the mosquito brain is wired to detect human odorants. We determined that the breath volatile carbon dioxide (CO_2) is detected by the largest unit of olfactory coding in the primary olfactory processing center of the mosquito brain, the antennal lobe. Synergistically, CO_2 detection gates synaptic transmission from defined populations of olfactory sensory neurons, innervating unique antennal lobe regions tuned to the human sweat odorant L-(+)-lactic acid. Our data suggests that simultaneous detection of signature human volatiles rapidly disinhibits a multimodal olfactory network for hunting humans in the mosquito brain.

Main Text:

Blood-thirsty female *A. aegypti* mosquitoes detect and navigate towards a plethora of physical and chemosensory cues emitted by the human body (*1-4*). Of these cues, human scent is a powerful mosquito attractant, comprising of a complex bouquet of hundreds of volatile chemicals derived from sweat, breath and the human skin microbiome (*5*). Despite recent advances in our understanding of mosquito chemoreception at the periphery (*2, 6-13*), central mechanisms involved in detection and integration of human body odorants by this prolific disease vector are largely unknown (*2*). This highlights the critical need for novel approaches to illuminate olfactory circuits underlying the epidemiologically important process of *A. aegypti* attraction to human body odor.

The olfactory system of *A. aegypti* consists of three major olfactory appendages including the antennae, maxillary palps and labella of the proboscis. Lining these organs are various morphological classes of porous sensilla (*14-16*) that house the dendritic processes of typically 2-3 olfactory sensory neurons (OSNs) that detect diverse structural classes of volatile odorants. The axonal processes of OSNs project to the primary olfactory processing brain center known as the antennal lobe (*17*). In related insects such as *Drosophila*, olfactory information is locally processed and encoded in the antennal lobe via the action of excitatory and inhibitory local neurons (*18-20*), before being sent by projection neurons to higher order brain centers involved in orchestrating innate and learned olfactory behaviors (*21-23*).

Large chemoreceptor gene families implicated in detection of various components of human scent and other ethologically relevant odorants are encoded in the *A. aegypti* genome (*24*). The Odorant Receptor (*OR*) chemoreceptor family, typically tuned to aldehydes, short-chain alcohols and ketones, likely mediates anthropophilic host preference in *A. aegypti* (*8, 12*). In a complementary fashion, chemoreceptors from the Ionotropic Receptor (*IR*) family that are responsive to carboxylic acids and amines (*25*), and certain Gustatory Receptors (*GR*) family members that detect the volatile gas carbon dioxide (CO_2) (*2*), drive synergistic behavioral taxis of female mosquitoes towards human scent (*26, 27*). For instance, L-(+)-lactic Acid, a predominant chemical fraction of human sweat, is alone unattractive to *A. aegypti*, but potently synergizes with CO_2 to elicit olfactory attraction when these two stimuli are combined together (*28, 29*). Functionality of the *IR* co-receptor *IR8a* that putatively forms multimeric *IR* complexes tuned to L-(+)-lactic acid and related acidic volatiles (*25*), as well as the *Gr1/2/3* CO_2 receptor complex (*2*), are together required

for this olfactory synergism. However, the mechanistic basis of how these and other human volatiles are integrated by the *A. aegypti* antennal lobe to yield attractive behavioral synergy is currently unclear.

To identify antennal lobe circuits mediating synergy between CO_2 and L-(+)-lactic acid in the mosquito brain, we first developed an updated *in vitro* neuroanatomical atlas of the antennal lobe from the *LVPib12 A. aegypti* strain, demonstrating that this olfactory brain center contains ~ 80 units of glomerular synaptic connectivity (*17*). In *Drosophila*, the axonal processes of OSNs expressing unique complements of chemoreceptors project from the peripheral sensory appendages such as the antenna and maxillary palp to spatially defined glomeruli within the antennal lobe (*30, 31*). To facilitate in-depth neuroanatomical studies and genetic access to the *A. aegypti* antennal lobe, we first applied CRISPR-Cas9 genome engineering (*32*) and *Mos1-mariner* transposition (*33*) to integrate components of the *QF2/QUAS* system (*34*) for binary expression of reporter transgenes in defined subsets of *A. aegypti* OSNs projecting to this brain region.

To generate transgenic *A. aegypti* chemoreceptor-*QF2* driver lines, we used CRISPR-Cas9 mediated homologous recombination to insert a *T2A-QF2* in-frame fusion cassette (*35*) into the coding exons of three major olfactory co-receptor genes: Odorant Receptor co-receptor (*orco*), Ionotropic Receptor co-receptor *IR8a*, and the CO_2 receptor complex subunit *Gr1* (Fig. 1A-C). Using this strategy, *QF2* was integrated in-frame into Exon 3 of each target gene, placing expression of this transcription factor under control of endogenous regulatory elements for each locus. These driver lines also included a visible *3xP3-DsRed2* eye marker to facilitate identification of transgenic individuals. $orco^{QF2Red}$ and $IR8a^{QF2Red}$ cassettes inserted in-frame as expected via ends-out recombination events, whereas $Gr1^{QF2Red}$ inserted in-frame yet also incorporated a duplicated copy of the plasmid backbone downstream of the *T2A-QF2* in-frame fusion via an ends-in recombination event.

We crossed each driver line with a *QUAS-mCD8::GFP* responder strain that we generated by *Mos1 mariner* transposition and demonstrated that we successfully labeled OSNs with membrane-tethered green fluorescent protein (GFP). Confocal analyses of female peripheral sensory appendages revealed strong GFP expression in OSN dendrites and cell bodies on the antenna, maxillary palp and labella of the proboscis of $orco^{QF2Red}$*>15XQUAS-mCD8::GFP* individuals (Fig. 1a and Fig. S1 a-e); as well as OSN labeling of the antennal flagellum of

103 *IR8a^{QF2Red}>15XQUAS-mCD8::GFP* (Fig. 1b) individuals, and maxillary palp tissue of
104 *Gr1^{QF2Red}>15XQUAS-mCD8::GFP* mosquitoes (Fig. 1c).
105
106 Expression patterns from *QF2* knock-ins were consistent with a previous *LVPib12* strain
107 neurotranscriptome analysis (*36*) that revealed broad *orco* expression across olfactory tissues,
108 with *IR8a* and *Gr1* expression confined to antennal and maxillary palp tissue, respectively.
109 Dendrites of *orco* (+) neurons on the mosquito antenna were localized to hair-like trichoid sensilla
110 (Fig. 1a), whereas dendrites of *IR8a* (+) neurons were confined to grooved-peg sensilla on the
111 antenna, and *Gr1* (+) neurons were found in capitate peg sensilla on the maxillary palp (Fig. 1b
112 and c). These latter two classes of sensilla are the locations for OSN-based detection of L-(+)-
113 lactic acid (*37, 38*) and CO_2 (*2, 39, 40*), respectively, grossly validating the neuroanatomical
114 specificity of our transgenic labeling approach.
115
116 To examine central projection patterns of OSNs expressing the CO_2 receptor complex subunit
117 *Gr1*, as well as *IR8a* (+) and *orco* (+) OSNs into the central nervous system, we dissected brains
118 from adult female mosquitoes and performed immunohistochemistry analyses with a primary
119 antibody directed against the pre-synaptic protein Bruchpilot (BRP) (*41*) to demarcate glomerular
120 boundaries of neuropils in the antennal lobe, and anti-GFP antibody to amplify mCD8::GFP signal.
121 Surprisingly, immunohistochemistry with *QF2^{Red}* genotypes revealed spurious red and green
122 fluorescence throughout the central brain (Fig. S2 a-c), particularly in glia, including in fixed brains
123 not subjected to anti-GFP staining, suggesting potential interference in the expected *QF2/QUAS*
124 transactivation pattern at these loci. As all of our *T2A-QF2* insertions included a downstream
125 fluorescent marker cassette containing the *3xP3* synthetic promoter (*42*), which is a multimerized
126 binding site for the paired-box transcription factor *Pax6* involved in glial and neuronal development
127 (*43, 44*), we suspected that the source of the this aberrant expression pattern may be due to
128 promiscuous *3xP3* enhancer activity operating at these genomic loci.
129
130 To abrogate this effect, we developed a strategy to excise floxed *3xP3* fluorescent marker
131 cassettes from our *QF2^{Red}* strains via crossing these genotypes to a germline *Cre* recombinase
132 strain (*exu-Cre*) that we engineered. Using this approach, we successfully generated marker-free
133 driver strains (*orco^{QF2}*, *IR8a^{QF2}* and *Gr1^{QF2}*) which were devoid of all *3xP3* fluorescent markers
134 and any apparent background fluorescence in the central brain, clearly driving reporter expression
135 in OSN axonal processes innervating the antennal lobe (Fig. 1, d-f and Fig. S2 d-i). Consistent
136 with peripheral expression patterns, in marker-free *QF2>mCD8:GFP* composite genotypes, *orco*

(+) OSNs were observed to innervate the largest number of glomeruli (60/78 total) across several spatial regions of the antennal lobe, whereas *IR8a* (+) neurons (15/78 total) and *Gr1* (+) neurons (1/78 total) innervate sparser subsets of glomeruli in posterolateral and mediodorsal antennal lobe regions, respectively (Fig. 2a).

Using a systematic reference key for *A. aegypti* antennal lobe nomenclature (*17*), we then determined that a subset of 6 *orco*/*IR8*a glomeruli had putative co-labeling, indicative of co-expression of these two genes, based on their overlapping positions and assigned name relative to defined antennal lobe landmarks. We also found 8/78 total glomeruli in the ventral region of the antennal lobe that were not labeled by any of these chemoreceptor driver lines (Fig. 2a), and we suggest these glomeruli may receive innervations from OSNs expressing other chemoreceptors such as those complexed with *IR* co-receptors *IR25a* and *IR76b*, which are known to project to the antennal lobe in *Drosophila* (*45*). Additionally, we visualized *orco* (+) neurons innervating the taste center of the insect brain known as the suboesophageal zone (SEZ) (Fig. S3), consistent with the projection pattern of *orco* (+) OSNs in the African malaria mosquito *Anopheles gambiae* (*46*). 2D and 3D mapping of antennal lobes from replicate brain samples (Fig 2, Fig. S4-S7) , revealed the same complement of glomeruli was consistently labeled across *orco*, *IR8a* and *Gr1* driver strains. Volumetric analysis of *A. aegypti* antennal lobe glomeruli from each of these clusters of chemoreceptor innervation further revealed that the *Gr1* (+) glomerulus MD1 is the largest glomerulus in the antennal lobe (Fig. 2b). This observation may reflect the critical importance of CO_2 to multiple facets of *A. aegypti* host-seeking behavior (*1-4, 26, 27*).

Markedly increased glomerular subdivision of the *A. aegypti* antennal lobe relative to *Drosophila* (*17*) makes assigning odor-evoked neurophysiological responses to particular glomeruli at high-spatial resolution a daunting challenge. To leverage the detailed receptor-to-glomerulus antennal lobe reference maps we generated for *orco* (+), *IR8a* (+) and *Gr1* (+) OSNs (Fig 2 and Fig. S4-S7), we next applied functional imaging assays with calcium modulated photoactivatable ratiometric indicator (CaMPARI2) (*47*) to assess neural correlates of olfactory synergy between CO_2 and L-(+)-lactic acid. This genetically encoded, ratiometric calcium indicator photoconverts from green to red in the presence of 405nm light and high levels of calcium (*47, 48*), providing a permanent readout of neural activity during odorant stimulation. CaMPARI2 is further amenable to post-hoc staining methods for spatial registration of neural activity (*47*). We localized photoconversion signal from this fluorescent indicator to specific antennal lobe glomeruli using brain co-staining with fluorophore-conjugated phalloidin toxin to mark cytoskeletal F-actin

171 filaments in OSN axonal processes (*49*), with reference to phalloidin-stained antennal lobe maps
172 that we generated (Fig. S8).
173
174 To initially trial the efficacy of CaMPARI2 at recording odor-evoked activity from *A. aegypti*
175 antennal lobe glomeruli, we calculated photoconversion ratios in the axon terminals of *Gr1* (+)
176 OSNs innervating the MD1 glomerulus in response to stimulation with CO_2. To do this, we first
177 generated composite imaging strains that express *CaMPARI2* driven by a cumulative 30 copies
178 of the Q upstream activation sequence in *Gr1* (+) OSNs (denoted here as $Gr1^{QF2}$ > *30XQUAS-*
179 *CaMPARI2*, Table S10). The olfactory appendages of live head-tethered mosquito preparations,
180 with surgically exposed antennal lobes, were then subjected to a standard CaMPARI stimulus
181 duty cycle (*48*) consisting of simultaneous pulses of 405nm photoconversion light through a high-
182 numerical aperture water immersion objective and 1% CO_2 delivered by a custom olfactometer.
183 After each photoconversion regime, brains were immediately dissected from each mosquito, co-
184 stained with fluorophore-conjugated toxin phalloidin to demarcate glomerular boundaries with
185 confocal imaging, and green to red CaMPARI2 photoconversion ratios in MD1 were calculated to
186 query whether the axonal terminals of *Gr1* (+) OSNs projecting to this glomerulus responded to
187 the stimulus. Encouragingly, MD1 exhibited a significantly higher rate of CaMPARI2
188 photoconversion in CO_2-stimulated mosquitoes versus those that were stimulated with synthetic
189 air (Fig. 3 a-c), further validating the ability of 405nm light to penetrate mosquito brain tissue and
190 photoconvert glomeruli such as MD1 positioned deep below the antennal lobe surface (*17*).
191
192 Having demonstrated CAMPARI2 photoconversion was a viable approach for activity-dependent
193 neural labeling in OSN axon terminals innervating the antennal lobe, we then went on to test
194 whether synergy between the sweat odorant L-(+)-lactic acid and CO_2 could be detected in
195 specific *IR8a* (+) glomeruli, given that *IR8a* (*25*) and the CO_2 receptor pathways (*2*) are both
196 required for synergistic attraction of *A. aegypti* to these two odorants. To do this, we mapped
197 CaMPARI2 activity in 12 *IR8a* (+) glomeruli in replicate brain samples derived from $IR8a^{QF2}$ >
198 *30XQUAS-CaMPARI2* mosquitoes that were stimulated with unitary and binary combinations of
199 L-(+)-lactic acid and CO2. Surprisingly, we determined that application of L-(+)-lactic acid alone
200 to olfactory appendages of live imaging mosquitoes did not yield higher CaMPARI2
201 photoconversion ratios than CO2 or synthetic air controls in *IR8a* (+) glomeruli (Fig. 4 b, c, d). In
202 contrast, we observed a dramatic increase in CaMPARI2 photoconversion ratios when CO_2 was
203 coapplied with L-(+)-lactic acid to mosquitoes (Fig. 4 a). In particular, two out of twelve *IR8a* (+)
204 glomeruli, denoted PL5 and PL6, exhibited synergistic and highly significant differences in mean

CaMPARI2 photoconversion values when co-stimulated with CO_2 and L-(+)-lactic acid relative to L-(+)-lactic acid or CO_2 alone and synthetic air controls (Fig. 4 e and f, Fig. S9 and S10). We interpret this as evidence that presynaptic calcium levels are significantly elevated in *IR8a* (+) OSN axon terminals innervating PL5 and PL6 in response to co-stimulation with CO_2 and L-(+)-lactic acid.

This study lays the critical foundation towards defining how constituents of human scent and other chemosensory stimuli are encoded in the mosquito brain. Our data are highly suggestive of the existence of a circuit-based mechanism for olfactory synergism between the human sweat odorant L-(+)-lactic acid and breath volatile CO_2 at first olfactory synapse in the antennal lobe. We observed that axon terminals of *IR8a* (+) neurons had consistently low CaMPARI2 photoconversion signals in response to stimulation with L-(+)-lactic acid or CO2 alone, that were not significantly different from baseline values observed with clean air. Synergistically, pre-synaptic calcium levels in axon terminals of *IR8a* (+) neurons were dramatically elevated upon co-stimulation of mosquitoes with L-(+)-lactic acid with CO_2, as reported by enhanced CaMPARI2 photoconversion in PL5 and PL6 glomeruli.

Previous extracellular recordings on the *A. aegypti* antenna demonstrated no changes in odor-evoked activity from L-(+)-lactic acid-sensitive OSNs in response to stimulation with this carboxylic acid with CO_2 (*38*) indicating synergism likely does not occur though peripheral mechanisms (*50, 51*) during ligand detection by OSN dendrites. Rather, we speculate given the silent nature of *IR8a* (+) glomerular responses towards unitary blends of either ligand, that this binary synergy may occur via disinhibitory local circuitry (*52*) operating between the CO_2-sensitive glomerulus MD1 and axon terminals of lactic acid-sensitive *IR8a* (+) glomeruli such as PL5 and PL6 in the antennal lobe.

Rapid central feedback between antennal lobe glomeruli to yield disinhibition of OSN axon terminals may therefore represent a simple, yet flexible circuit for this prolific disease vector to faithfully identify signature combinations of human odorants and improve the fidelity of their hunt for humans. Given that multiple human odorants in combination likely lie at the heart of mosquito lust for human scent (*53, 54*), further dissection of synergistic coding operational in the mosquito antennal lobe may reveal key human volatiles and mosquito chemosensory circuitry that can be targeted to combat mosquito-borne diseases such as dengue, Zika and malaria.

239 **References:**

240

241 1. R. A. Corfas, L. B. Vosshall, The cation channel TRPA1 tunes mosquito thermotaxis to
242 host temperatures. *Elife* **4**, (2015).
243 2. C. J. McMeniman, R. A. Corfas, B. J. Matthews, S. A. Ritchie, L. B. Vosshall, Multimodal
244 integration of carbon dioxide and other sensory cues drives mosquito attraction to
245 humans. *Cell* **156**, 1060-1071 (2014).
246 3. F. van Breugel, J. Riffell, A. Fairhall, M. H. Dickinson, Mosquitoes Use Vision to
247 Associate Odor Plumes with Thermal Targets. *Curr Biol* **25**, 2123-2129 (2015).
248 4. C. Vinauger *et al.*, Visual-Olfactory Integration in the Human Disease Vector Mosquito
249 Aedes aegypti. *Curr Biol* **29**, 2509-2516.e2505 (2019).
250 5. L. Dormont, J. M. Bessière, A. Cohuet, Human skin volatiles: a review. *J Chem Ecol* **39**,
251 569-578 (2013).
252 6. A. F. Carey, G. Wang, C. Y. Su, L. J. Zwiebel, J. R. Carlson, Odorant reception in the
253 malaria mosquito Anopheles gambiae. *Nature* **464**, 66-71 (2010).
254 7. Z. Chen, F. Liu, N. Liu, Human Odour Coding in the Yellow Fever Mosquito, Aedes
255 aegypti. *Sci Rep* **9**, 13336 (2019).
256 8. M. DeGennaro *et al.*, orco mutant mosquitoes lose strong preference for humans and
257 are not repelled by volatile DEET. *Nature* **498**, 487-491 (2013).
258 9. E. A. Hallem, A. Nicole Fox, L. J. Zwiebel, J. R. Carlson, Olfaction: mosquito receptor for
259 human-sweat odorant. *Nature* **427**, 212-213 (2004).
260 10. W. D. Jones, P. Cayirlioglu, I. G. Kadow, L. B. Vosshall, Two chemosensory receptors
261 together mediate carbon dioxide detection in Drosophila. *Nature* **445**, 86-90 (2007).
262 11. T. Lu *et al.*, Odor coding in the maxillary palp of the malaria vector mosquito Anopheles
263 gambiae. *Curr Biol* **17**, 1533-1544 (2007).
264 12. C. S. McBride *et al.*, Evolution of mosquito preference for humans linked to an odorant
265 receptor. *Nature* **515**, 222-227 (2014).
266 13. G. Wang, A. F. Carey, J. R. Carlson, L. J. Zwiebel, Molecular basis of odor coding in the
267 malaria vector mosquito Anopheles gambiae. *Proc Natl Acad Sci U S A* **107**, 4418-4423
268 (2010).
269 14. S. B. McIver, Structure of sensilla trichodea of female Aedes aegypti with comments on
270 innervation of antennal sensilla. *Journal of Insect Physiology* **24**, 383-390 (1978).
271 15. S. B. McIver, Fine structure of pegs on the palps of female culicine mosquitoes. *Can J*
272 *Zool* **50**, 571-576 (1972).
273 16. S. B. McIver, Fine structure of antennal sensilla coeloconica of culicine mosquitoes.
274 *Tissue Cell* **5**, 105-112 (1973).
275 17. S. Shankar, C. J. McMeniman, An updated antennal lobe atlas for the yellow fever
276 mosquito Aedes aegypti. *PLoS Negl Trop Dis* **14**, e0008729 (2020).
277 18. Y. H. Chou *et al.*, Diversity and wiring variability of olfactory local interneurons in the
278 Drosophila antennal lobe. *Nat Neurosci* **13**, 439-449 (2010).
279 19. E. J. Hong, R. I. Wilson, Simultaneous encoding of odors by channels with diverse
280 sensitivity to inhibition. *Neuron* **85**, 573-589 (2015).
281 20. E. Yaksi, R. I. Wilson, Electrical coupling between olfactory glomeruli. *Neuron* **67**, 1034-
282 1047 (2010).
283 21. S. J. Caron, V. Ruta, L. F. Abbott, R. Axel, Random convergence of olfactory inputs in
284 the Drosophila mushroom body. *Nature* **497**, 113-117 (2013).
285 22. M. J. Dolan *et al.*, Neurogenetic dissection of the Drosophila lateral horn reveals major
286 outputs, diverse behavioural functions, and interactions with the mushroom body. *Elife* **8**,
287 (2019).

23. V. Grabe *et al.*, Elucidating the Neuronal Architecture of Olfactory Glomeruli in the Drosophila Antennal Lobe. *Cell Rep* **16**, 3401-3413 (2016).
24. B. J. Matthews *et al.*, Improved reference genome of Aedes aegypti informs arbovirus vector control. *Nature* **563**, 501-507 (2018).
25. J. I. Raji *et al.*, Aedes aegypti Mosquitoes Detect Acidic Volatiles Found in Human Odor Using the IR8a Pathway. *Curr Biol* **29**, 1253-1262.e1257 (2019).
26. T. Dekker, R. T. Cardé, Moment-to-moment flight manoeuvres of the female yellow fever mosquito (Aedes aegypti L.) in response to plumes of carbon dioxide and human skin odour. *J Exp Biol* **214**, 3480-3494 (2011).
27. T. Dekker, M. Geier, R. T. Cardé, Carbon dioxide instantly sensitizes female yellow fever mosquitoes to human skin odours. *J Exp Biol* **208**, 2963-2972 (2005).
28. F. Acree, Jr., R. B. Turner, H. K. Gouck, M. Beroza, N. Smith, L-Lactic acid: a mosquito attractant isolated from humans. *Science* **161**, 1346-1347 (1968).
29. A. E. Eiras, P. C. Jepson, Host location by Aedes aegypti (Diptera: Culicidae): a wind tunnel study of chemical cues. *Bulletin of Entomological Research* **81**, 151-160 (1991).
30. A. Couto, M. Alenius, B. J. Dickson, Molecular, anatomical, and functional organization of the Drosophila olfactory system. *Curr Biol* **15**, 1535-1547 (2005).
31. L. B. Vosshall, A. M. Wong, R. Axel, An olfactory sensory map in the fly brain. *Cell* **102**, 147-159 (2000).
32. K. E. Kistler, L. B. Vosshall, B. J. Matthews, Genome engineering with CRISPR-Cas9 in the mosquito Aedes aegypti. *Cell Rep* **11**, 51-60 (2015).
33. C. J. Coates, N. Jasinskiene, L. Miyashiro, A. A. James, Mariner transposition and transformation of the yellow fever mosquito, Aedes aegypti. *Proc Natl Acad Sci U S A* **95**, 3748-3751 (1998).
34. O. Riabinina *et al.*, Improved and expanded Q-system reagents for genetic manipulations. *Nat Methods* **12**, 219-222, 215 p following 222 (2015).
35. F. Diao, B. H. White, A novel approach for directing transgene expression in Drosophila: T2A-Gal4 in-frame fusion. *Genetics* **190**, 1139-1144 (2012).
36. B. J. Matthews, C. S. McBride, M. DeGennaro, O. Despo, L. B. Vosshall, The neurotranscriptome of the Aedes aegypti mosquito. *BMC Genomics* **17**, 32 (2016).
37. E. E. Davis, Structure-response relationship of the lactic acid-excited neurones in the antennal grooved-peg sensilla of the mosquito Aedes aegypti. *Journal of Insect Physiology* **34**, 443-449 (1988).
38. E. E. Davis, P. G. Sokolove, Lactic acid-sensitive receptors on the antennae of the mosquito,Aedes aegypti. *Journal of comparative physiology* **105**, 43-54 (1976).
39. A. J. Grant, B. E. Wigton, J. G. Aghajanian, R. J. O'Connell, Electrophysiological responses of receptor neurons in mosquito maxillary palp sensilla to carbon dioxide. *J Comp Physiol A* **177**, 389-396 (1995).
40. F. E. Kellogg, Water vapour and carbon dioxide receptors in Aedes aegypti. *J Insect Physiol* **16**, 99-108 (1970).
41. A. Hofbauer *et al.*, The Wuerzburg hybridoma library against Drosophila brain. *J Neurogenet* **23**, 78-91 (2009).
42. A. J. Berghammer, M. Klingler, E. A. Wimmer, A universal marker for transgenic insects. *Nature* **402**, 370-371 (1999).
43. R. Quiring, U. Walldorf, U. Kloter, W. J. Gehring, Homology of the eyeless gene of Drosophila to the Small eye gene in mice and Aniridia in humans. *Science* **265**, 785-789 (1994).
44. T. Suzuki, R. Takayama, M. Sato, eyeless/Pax6 controls the production of glial cells in the visual center of Drosophila melanogaster. *Dev Biol* **409**, 343-353 (2016).
45. A. F. Silbering *et al.*, Complementary function and integrated wiring of the evolutionarily distinct Drosophila olfactory subsystems. *J Neurosci* **31**, 13357-13375 (2011).

46. O. Riabinina *et al.*, Organization of olfactory centres in the malaria mosquito Anopheles gambiae. *Nat Commun* **7**, 13010 (2016).
47. B. Moeyaert *et al.*, Improved methods for marking active neuron populations. *Nat Commun* **9**, 4440 (2018).
48. B. F. Fosque *et al.*, Neural circuits. Labeling of active neural circuits in vivo with designed calcium integrators. *Science* **347**, 755-760 (2015).
49. W. Rössler, J. Kuduz, F. W. Schürmann, D. Schild, Aggregation of f-actin in olfactory glomeruli: a common feature of glomeruli across phyla. *Chem Senses* **27**, 803-810 (2002).
50. C. Y. Su, K. Menuz, J. Reisert, J. R. Carlson, Non-synaptic inhibition between grouped neurons in an olfactory circuit. *Nature* **492**, 66-71 (2012).
51. L. Xu *et al.*, Widespread receptor-driven modulation in peripheral olfactory coding. *Science* **368**, eaaz5390 (2020).
52. W. Zhao *et al.*, A disinhibitory mechanism biases Drosophila innate light preference. *Nat Commun* **10**, 124 (2019).
53. U. R. Bernier *et al.*, Synergistic attraction of Aedes aegypti (L.) to binary blends of L-lactic acid and acetone, dichloromethane, or dimethyl disulfide. *J Med Entomol* **40**, 653-656 (2003).
54. R. C. Smallegange, Y. T. Qiu, J. J. van Loon, W. Takken, Synergism between ammonia, lactic acid and carboxylic acids as kairomones in the host-seeking behaviour of the malaria mosquito Anopheles gambiae sensu stricto (Diptera: Culicidae). *Chem Senses* **30**, 145-152 (2005).
55. V. Nene *et al.*, Genome sequence of Aedes aegypti, a major arbovirus vector. *Science* **316**, 1718-1723 (2007).
56. M. Li *et al.*, Germline Cas9 expression yields highly efficient genome engineering in a major worldwide disease vector, Aedes aegypti. *Proc Natl Acad Sci U S A* **114**, E10540-e10549 (2017).
57. C. J. Potter, L. Luo, Splinkerette PCR for mapping transposable elements in Drosophila. *PLoS One* **5**, e10168 (2010).
58. J. M. Richardson, S. D. Colloms, D. J. Finnegan, M. D. Walkinshaw, Molecular architecture of the Mos1 paired-end complex: the structural basis of DNA transposition in a eukaryote. *Cell* **138**, 1096-1108 (2009).
59. K. W. Beyenbach, R. Masia, Membrane conductances of principal cells in Malpighian tubules of Aedes aegypti. *J Insect Physiol* **48**, 375-386 (2002).

Acknowledgements:

We thank N. Kizito, B. Natarajan, H. Rosado, M. Gebhardt, V. Balta and B. Burgunder for expert technical assistance; R. Harrell (UM-ITF) for mosquito embryonic microinjection services; S. Seo and A. Hammond for help with transgene mapping, C. Potter and E. Schreiter for constructs and technical advice; and C. Huang, M. Schnitzer, B. Ferris, G. Maimon, C. Dan and V. Jayaraman for guidance on surgical preparations. This research was supported by funding from the National Institutes of Health NIAID (R21 AI139358-01), USAID (AID-OAA-F-16-00061) and Centers for Disease Control and Prevention (200-2017-93143) to C.J.M; and funding to G.M.T. as a postdoctoral fellow on The Molecular And Cellular Basis Of Infectious Diseases (MCBID) Program (T32A1007417) from the NIH. O.S.A and M.L. were supported in part by a DARPA Safe Genes Program Grant (HR0011-17-2-0047) and a DARPA ReVector program grant (HR0011-20-2-0030) awarded to O.S.A. The views, opinions and/or findings expressed should not be interpreted as representing the official views or policies of the Department of Defense or the U.S. Government. Microscopy infrastructure at Johns Hopkins School of Medicine Microscope Core Facility used in this research was supported by the National Institutes of Health NCRR (S10OD016374 and S10OD023548). The mosquito template in Figure 1 was created for us by Biorender.com. We thank Terry Shelley at the JHU Center for Neuroscience Research Machine Shop for fabrication services supported by NINDS Center grant (NS050274). We further acknowledge generous support to C.J.M. from Johns Hopkins Malaria Research Institute (JHMRI) and Bloomberg Philanthropies. S.S. and G.M.T. were supported by JHMRI Postdoctoral Fellowships.

Contributions:

S.S. and C.J.M conceived the experimental design. M.L. and O.S.A. generated and provided the *exu-Cas9* strain for use. G.M.T., C.J.M. and S.S. together engineered constructs for transgenesis and the custom olfactometer for odorant delivery. C.J.M. and G.M.T. screened, genotyped and maintained transgenic lines. E.D.S. performed confocal analyses of *IR8a* peripheral expression patterns. S.S. performed all other microscopy, immunohistochemistry, antennal lobe reconstructions, glomerular mapping and *CaMPARI2* imaging experiments. D.G. and S.S. analyzed the data. S.S. and C.J.M. drafted the manuscript.

Competing interests:

The authors declare no competing interests.

Materials & Correspondence: Correspondence to Conor J. McMeniman

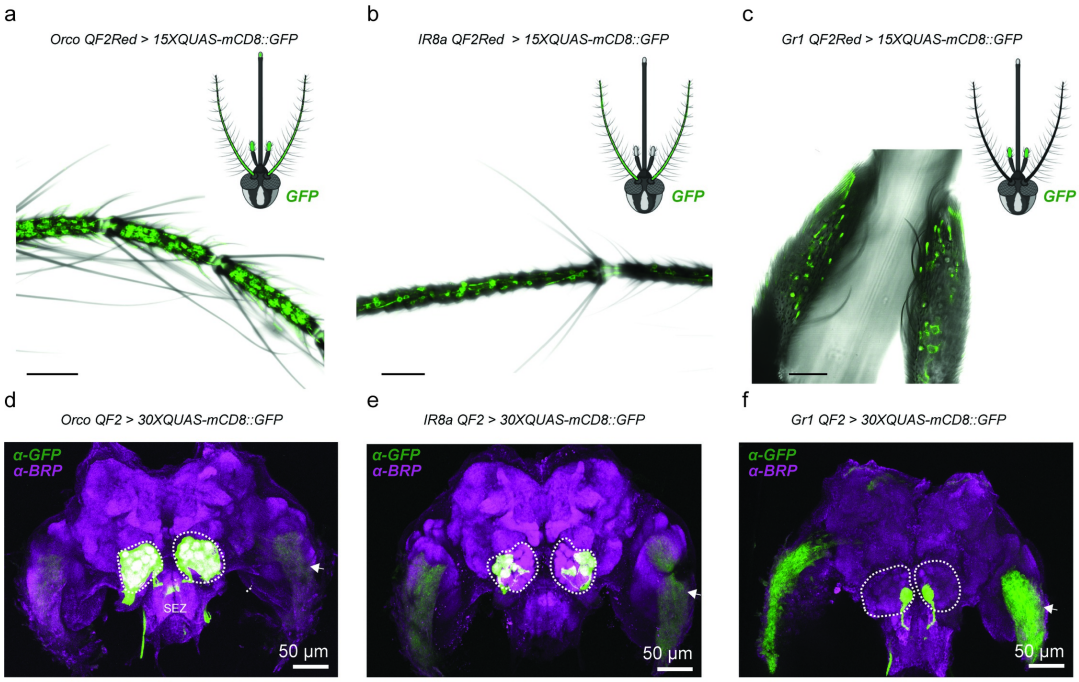

Figure 1. OSNs expressing divergent chemoreceptor gene families project centrally to defined regions of the *Aedes aegypti* antennal lobe. To study the expression patterns of *orco*, *IR8a* and *Gr1* in the nervous system of female *A. aegypti*, each of the three chemoreceptor *QF2* driver lines we generated was crossed to a *QUAS mCD8::GFP* reporter line and peripheral and central innervation patterns were imaged using confocal microscopy. **(a)** Densely packed cell bodies of *orco* (+) OSNs were observed in all 13 antennal flagellomeres, with dendrites localized to trichoid sensilla along the antennal surface, as well as the sensilla on the labella of the proboscis and maxillary palps (see Figure S1); **(b)** *IR8a* (+) OSNs were housed on all antennal flagellomeres in grooved peg sensilla; while **(c)** *Gr1* (+) OSNs were visualized exclusively in the club-shaped capitate peg sensilla on the ventral surface of the maxillary palps. Projections to the mosquito brain: **(d)** *orco* (+) neurons innervate the entire anterior region of the antennal lobe as well as the suboesophageal zone (SEZ), located ventral to the antennal lobe; **(e)** *IR8a* (+) neurons from the antenna innervate a group of glomeruli in the posterolateral and central region of the antennal lobe; while **(f)** *Gr1* (+) neurons originating from the maxillary palps uniquely innervate a single large glomerulus, found in the posterior region of the antennal lobe. Maximum intensity projections (d-e) and a single posterior z-slice (f) for the anterior view of adult female mosquito brains are shown at 10X magnification. The antennal lobes are encircled in white. Arrows indicate expression of the *3xP3-ECFP* marker in the outer optic lobes.

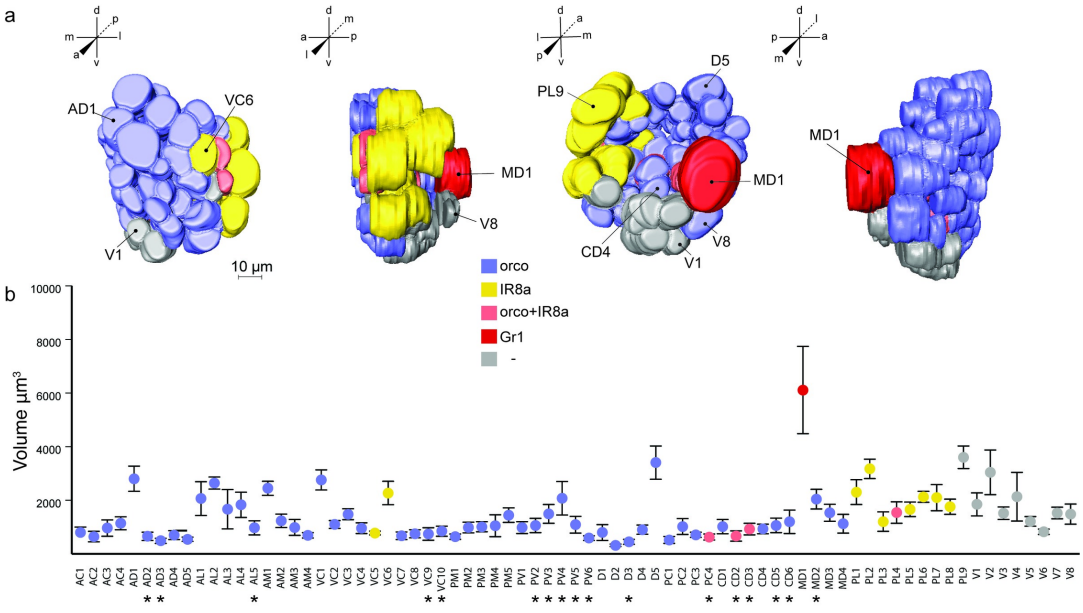

Figure 2. CO_2 receptor complex neurons innervate the largest glomerulus in the *Aedes aegypti* antennal lobe. **(a)** 3D reconstructed model of the left antennal lobe of a female *A. aegypti* mosquito as seen from the anterior, lateral, posterior and medial perspectives. On this model, 60 glomeruli innervated by *orco* (+) neurons are shaded blue, 15 glomeruli receiving projections from *IR8a* (+) neurons are shaded yellow, the MD1 glomerulus targeted by *Gr1* (+) neurons is shaded red. A group of 8 ventral glomeruli not innervated by any of the three classes of chemosensory neurons are shaded grey. Glomeruli putatively co-innervated by *orco* (+) and *IR8a* (+) neurons are shaded orange. Eight landmark glomeruli for spatial registration are shown on the model. These include AD1 and VC6, seen on the anterior surface, and MD1, V1, V8, PL9, CD4 and D5 on the posterior surface. Scale bar for 3D model: 10 µm. Template genotype: *orco^{QF2} > 30XQUAS-mCD8::GFP*. **(b)** Average volumes for 75 glomeruli that were consistently identified in antennal lobe reconstructions. Three glomeruli (D6, VC11 and VC12) could not be consistently identified across all reconstructions and thus were excluded from this volumetric analysis. Based on observed levels of GFP fluorescence throughout individual glomeruli, we classified the innervation pattern as being 'heavy' or 'sparse' with the latter glomeruli labeled by asterisks. MD1 innervated by *Gr1* (+) neurons is the largest antennal lobe glomerulus with a mean volume of approximately 6000 µm^3. Mean volumes +/- s.e.m. are plotted, *n* = 5 brains.

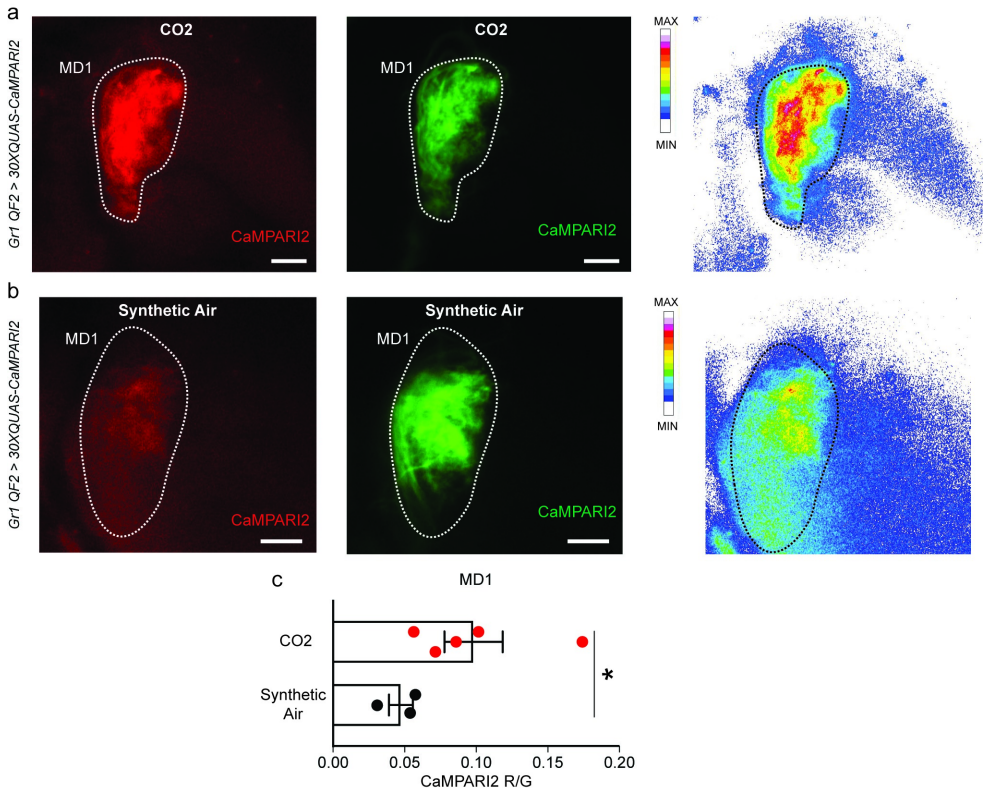

Figure 3: The *Aedes aegypti* MD1 glomerulus detects CO_2. Female *Gr1*^{QF2} > *30XCaMPARI2* mosquitoes were exposed to simultaneous pulses of 1% CO2 and 405nm photoconversion light, and post-stimulation brains were dissected to analyze activity-dependent neural labeling visualized by the ratiometric intensity of red to green CaMPARI2 fluorescence. **(a)** The MD1 glomerulus, receiving innervation from *Gr1* (+) maxillary palp neurons was strongly activated by CO_2, in contrast to **(b)** weak activity labeling in response to stimulation with synthetic air. **(c)** Mean CaMPARI2 photoconversion values were significantly different between CO_2 and control synthetic air conditions (P = 0.037 *, Mann-Whitney test, n = 3-5 brains per stimulus, mean R/G values +/- s.e.m. plotted). Green and Red *CaMPARI2* signal in MD1 are shown after odor stimulation. Red *CaMPARI2* in *IR8a* (+) glomeruli is visualized on the right panels as a heatmap of red fluorescence intensity. Dotted lines outline the boundary of the MD1 glomerulus. MD1 from the left antennal lobe was imaged at 63X magnification. Scale bars: 10 μm.

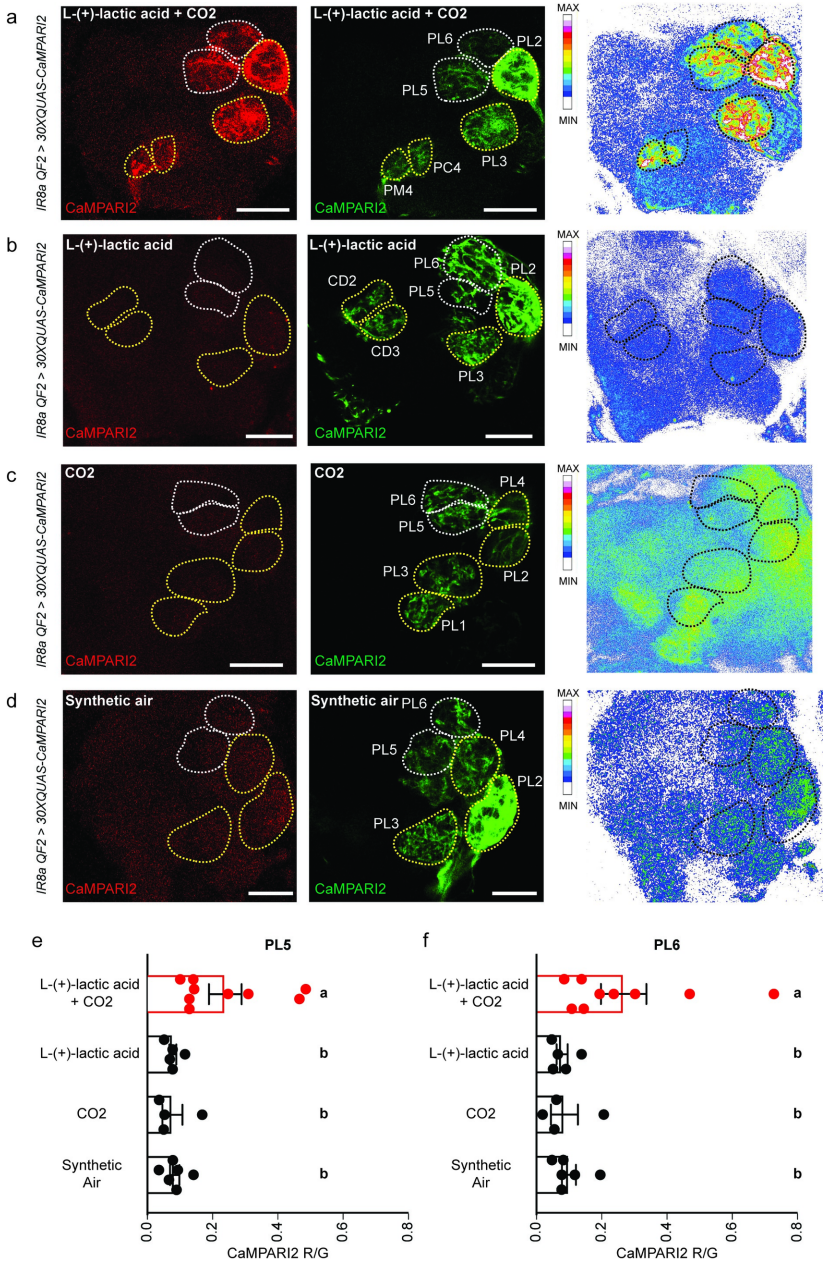

Figure 4: CO_2 and L-(+)-lactic acid co-stimulation synergistically gates pre-synaptic calcium levels in acid-sensing IR8a neurons. OSN axon terminals of *IR8a* (+) neurons innervating the antennal lobe exhibited strong CaMPARI2 photoconversion upon co-stimulation of female *IR8a*^{QF2} > *30XCaMPARI2* mosquitoes with simultaneous pulses of 1% CO_2 with L-(+)-lactic acid **(a).** In contrast mosquitoes stimulated with either odorant alone **(b - c)**, showed minimal photoconversion above background levels **(d)**. Glomeruli PL5 and PL6 were more significantly photoconverted in the presence of L-(+)-lactic acid and CO_2 relative to all other odor treatments (**e – f**) ($P < 0.05$ for all comparisons to L-(+)-lactic acid + CO_2, Tukey's Multiple Comparison Test, n = 4-9 brains per stimulus, mean R/G values +/- s.e.m. plotted). Additional glomeruli in the same z-plane were also noticeably activated in some replicates (see Fig. S9). Red *CaMPARI2* in *IR8a* (+) glomeruli is visualized on the right panels as a heatmap of red fluorescence intensity. Dotted outlines represent the boundaries of the *IR8a* (+) glomeruli in these representative z-slices. The *IR8a* (+) glomeruli from the left antennal lobe were imaged at 63X magnification. Scale bars: 10 µm.

SUPPLEMENTARY MATERIALS

Materials and Methods:

Mosquito Stock Maintenance

The *Aedes aegypti LVPib12* strain (*55*) was used as the recipient genetic background for the generation of all transgenic lines and subsequent assays. Mosquitoes were maintained with a 12 hr light:dark photoperiod at 27°C and 80% relative humidity using a standardized rearing protocol (*17*). All experiments were conducted with non-blood fed and mated *A. aegypti* females that were 5-10 day old. Adult mosquitoes were provided constant access to a 10% w/v sucrose solution.

Selection and *in vitro* transcription of sgRNAs

Single guide RNA (sgRNA) target sites in the coding sequences of *orco* (AAEL005776), *IR8a* (AAEL002922) and *Gr1* (AAEL002380) were identified using online design pipelines at http://zifit.partners.org/ZiFiT/ and http://crispr.mit.edu/. Candidate sgRNAs at each locus were prioritized for downstream use based on their putative lack of off-target activity in the *A. aegypti* genome. sgRNAs were transcribed and purified according to the method of Kistler et al. (2016) (*32*). Briefly, DNA templates for sgRNA synthesis were generated by PCR with two partially overlapping PAGE-purified oligos (IDT) for each target. sgRNA was subsequently produced using the MegaScript T7 in vitro transcription kit (Ambion) and purified using the MEGAclear transcription clean-up kit (Invitrogen). Prior to microinjection, sgRNA activity was confirmed by *in vitro* cleavage assays with purified recombinant Cas9 protein (PNA Bio, Inc., CP01-200) following the manufacturer's instructions. See Table S1 for final sgRNA sequences.

T2A-QF2 Donor Constructs

A base *T2A-QF2* donor construct (pBlackbird) for CRISPR-Cas9 mediated homologous recombination into target chemoreceptor loci in *A. aegypti* was generated by sequential rounds of In-Fusion cloning (TakaraBio). This construct was generated with a SwaI site for in-frame insertion of the 5′ homology region from a of a gene directly with the *T2A-QF2* coding sequence. To survey for homology arms, genomic DNA regions spanning each target site were first PCR amplified with CloneAmp (TakaraBio) using the following primers for *orco* (5'-TGCAAGTGGATCATTTGTCG-3' and 5'-GTGCAATTGTGCCATTTTGA-3'), *IR8a* (5'-CAAAGTATAATTTCGCCCCCTCC-3' and 5'-CTCTATGGCAGCCAAGATATTGG-3') and *Gr1* (5'-AAGCCAGCTGGAAGGACATA-3' and 5'-ACCGTTTGGAGGTTGAATTG-3'). PCR products

were cloned into pCR2.1-TOPO (Invitrogen) for subsequent sequence verification. After determining the most common sequence clone for each region, homology arms flanking the CRISPR-Cas9 cut site were then PCR-amplified and inserted into the pBlackbird donor at the SwaI site (5′ arm) and BssHII site (3′ arm) using the In-Fusion primers listed in Table S2, to generate a T2A-in frame fusion into the coding exon of interest. Three donor constructs that yielded successful integrations at these target loci included *pBlackbird-AaOrco-sg2*, *pBlackbird-AaIR8a-sg2* and *pBlackbird-AaGr1-sg2*. Each *T2A-QF2* donor construct included a floxed *3xP3-DsRed2* cassette as transformation marker, as well as a *3xP3-ECFP* cassette in the vector backbone outside the transposition cassette as a marker to assess putative ends-in recombination events at the target locus or alternate off-target integrations elsewhere in the genome.

Mos1 mariner QUAS Reporter and Germline _Cre_ Constructs

QUAS reporter and germline *Cre* cassettes were generated by sequential rounds of In-Fusion cloning (TakaraBio) into template plasmid backbones for *Mos1 mariner* transposition (*pMOS-3xP3-ECFP* and *pMOS-3xP3-dsRed*) (*33*) as outlined in Table S3. All *QUAS* reporter constructs included a *3xP3-ECFP* cassette to mark transformants, while the *pMOS* backbone for *QUAS-CaMPARI2* was modified to remove the existing *3xP3-DsRed2* cassette from that vector and replace it with floxed *3xP3-ECFP cassette.* The *pMOS* backbone for generating *exu*-Cre was modified to have a *Polyubiquitin-EYFP* marker using standard cloning methods. Final plasmids that yielded transformants included: *pMosECFP-QUAS-mCD8::GFP-p10*, *pMoslECFP-QUAS-CaMPARI2-p10* and *pMosEYFP-Exu-Cre-p10*.

The complete nucleotide sequences for all donor plasmids, *pMOS* vector backbones and *Mos1* helper (*33*) plasmids used in this study will be deposited to Addgene, and template materials are listed in Table S3.

Generation of Transgenic Lines

T2A-QF2 knock-in lines into *orco*, *Ir8a* and *Gr1* were generated via CRISPR-Cas9 mediated homologous recombination (*32*) using embryonic microinjection.

To generate the $Gr1^{QF2Red}$ insertion, an injection mixture consisting of sgRNA (40ng/ul), purified recombinant Cas9 protein (PNA Bio, 300ng/ul) and donor plasmid (500ng/ul) was prepared in microinjection buffer (5 mM KCl and 0.1 mM NaH2PO4, pH 7.2); and microinjected into the

539 posterior pole of pre-blastoderm stage *LVPib12* embryos of at the Insect Transformation Facility
540 at University of Maryland (UM-ITF) using standard methods.
541
542 To generate the *orco*^{QF2Red} and *IR8a*^{QF2Red} insertions, for each target *in vitro* transcribed sgRNA
543 (100ng/ul) was mixed T2A-QF2 donor construct (100 ng/ul) and microinjected in the McMeniman
544 laboratory into the posterior pole of transgenic *A. aegypti* pre-blastoderm stage embryos
545 expressing *Cas9* under the maternal germline promoter *exuperantia* (*56*). Transformed G_1 larvae
546 from all knock-in lines were isolated via the visible expression of *3xP3-DsRed2* fluorescent marker
547 in eye tissue and were outcrossed to the *LVPib12* wild-type line for at least five generations prior
548 to attempting to generate homozygous strains. Precise insertion of each donor construct was
549 confirmed by PCR amplification and subsequent Sanger sequencing of regions covering the
550 homology arms and flanking sequences on either side of the insertion.
551
552 *QUAS* reporter and *exu-Cre* strains were generated by co-injecting each *pMOS* donor construct
553 (500 ng/ul) with a pKhsp82 helper plasmid (300 ng/ul) expressing the Mos1 transposase (*33*) to
554 foster quasi-random integration into the genome. Embryo microinjections were carried out by UM-
555 ITF using standard techniques. For *QUAS* reporters, G_1 lines were selected for stock
556 establishment that had the strongest *3xP3-ECFP* expression levels in the eyes and ventral nerve
557 cord, indicative of responder loci accessible for neuronal expression.
558
559 ***Cre-LoxP* Mediated Excision of *3xP3* Fluorescent Markers**
560 To remove the floxed *3xP3-DsRed2* cassette from each driver line (*IR8a*^{QF2Red}, *orco*^{QF2Red},
561 *Gr1*^{QF2Red}), we crossed males of each *3xP3-DsRed2* marked *QF2* driver line to females of the
562 *exu-Cre* line we generated. We then screened F_1 progeny for loss of the *DsRed2* marker. In the
563 case of the *Gr1*^{QF2Red} line, the reduplicated marker due to the ends-in insertion was incompletely
564 removed in F_1 progeny, so progeny lacking visible *DsRed2* or *ECFP* markers were mated to their
565 *exu-Cre* (+) siblings to ensure complete excision of all markers. Precise excision was confirmed
566 for all three driver lines by PCR and Sanger sequencing using this strategy. Marker-free *QF2*
567 driver lines are denoted as *IR8a*^{QF2}, *orco*^{QF2} and *Gr1*^{QF2}.
568
569 ***Mos1 mariner* Splinkerette PCR**
570 *QUAS* and *Exu-Cre* transgenes inserted via *Mos1* mariner transposition were mapped to
571 chromosomal locations (AaegL5.0 genome assembly) using a modified Splinkerette PCR, based
572 on the protocol described in Potter and Luo (2010) (*57*). Genomic DNA from single transgenic

individuals was digested using the restriction enzymes BamHI-HF, BglII, and BstYI (New England BioLabs) in separate reactions; digests were left overnight (~16 hrs). BstYI reactions were subsequently heat-inactivated at 80° for 20 minutes according to the recommended protocol. BamHI reactions were purified using the QIAquick PCR Purification Kit (QIAgen) according to manufacturer instructions and eluted in 50 µl H_2O after 4 minutes of incubation at 50°C.

Digests of genomic DNA were ligated to annealed SPLNK oligos as described (*57*). Splinkerette oligonucleotides 5'-GATCCCACTAGTGTCGACACCAGTCTCTAA-TTTTTTTTTTCAAAAAAA-3' and 5'-CGAAGAGTAACCGTTGCTAGGAGAGACCGTGGCTG-AATGAGACTGGTGTCGACACTAGTGG-3' were first annealed and ligated to digested genomic DNA. The first- and second-round PCR amplification steps were modified, using the standard SPNLK primers and new primers designed to the inverted repeat regions of the *Mos1 mariner* transposon. PCR products were amplified using Phusion High-Fidelity DNA Polymerase (NEB).

First round Splinkerette PCR was carried out using the primers 5'-CGAAGAGTAACCGTTGCTAGGAGAGACC-3' and 5'-TCAGAGAAAACGACCGGAAT-3' for the right inverted repeat, and 5'-CGAAGAGTAACCGTTGCTAGGAGAGACC-3' and 5'-CACCACTTTTGAAGCGTTGA-3' for the left inverted repeat. The second round of Splinkerette PCR was carried out using the primers 5'-GTGGCTGAATGAGACTGGTGTCGAC-3' and 5'-TCCGATTACCACCTATTCGC-3' for the right inverted repeat, and 5'-GTGGCTGAATGAGACTGGTGTCGAC-3' and 5'-ATACTGTCCGCGTTTGCTCT-3' for the left inverted repeat. In the case of *QUAS-CaMPARI2*, the extension time of the second-round PCR was lengthened to 4 minutes to amplify longer segments of flanking DNA. PCR products were gel purified and Sanger sequenced with additional sequencing primers for the right (5'-AAAAATGGCTCGATGAATGG-3') and left (5'-GGTGGTTCGACAGTCAAGGT-3') inverted repeats. BLAST searches were used to map Splinkerette fragments derived from each *Mos1 mariner* cassette to coordinate locations in the genome at canonical TA dinucleotides (*58*) and insertion sites (Table S5) were subsequently confirmed by PCR.

Genotyping *Gr1*^{QF2Red} and *Gr1*^{QF2}

Gr1^{QF2Red} and *Gr1*^{QF2} knock-ins were genotyped using a multi-primer PCR assay with the forward primer: 5′-CATGTACATCCGCAAGTTGG-3′; and two standard reverse primers: 5′-TGTTAGTGAGATCAGCGAACCT-3′ and 5′-GATCAACCCACAGATGACGA-3′. Fragments for size-based genotyping were amplified via DreamTaq (Thermo Scientific) and analyzed by

conventional agarose gel electrophoresis. Each of the reverse primers were used at half the normal concentration. This resulted in a single 689 bp amplicon in homozygous mosquitoes; a single 884 bp amplicon in wild-type mosquitoes; and two amplicons, one at 689 bp and one at 884 bp, in heterozygous mosquitoes.

Genotyping *IR8a^{QF2Red}* and *IR8a^{QF2}*

IR8a^{QF2Red} and *IR8a^{QF2}* knock-ins were genotyped using a multi-primer PCR assay with the forward primer: 5′-AGGAGATTGCGCTTGTCCTA-3′; and two standard reverse primers: 5′-CCCCGACATAGTTGAGCATT-3′ and 5′-TGTTAGTGAGATCAGCGAACCT-3′. Each of the reverse primers were used at half the normal concentration. This resulted in a single 560 bp amplicon in homozygous mosquitoes, a single 501 bp amplicon in wild-type mosquitoes, and two amplicons, one at 560 bp and one at 501 bp, in heterozygous mosquitoes.

Genotyping *orco^{QF2Red}* and *orco^{QF2}*

orco^{QF2Red} and *orco^{QF2}* knock-ins were genotyped using conventional PCR. The PCR reaction used the forward primer: 5′-GCGATAGCGTCAAAAACGTA-3′ and reverse primer: 5′-ATTCCTTGAAGGTCCATTGCAG-3′. This resulted in an 1842 bp amplicon corresponding to the *orco^{QF2}* allele, a 3129 bp amplicon corresponding to the *orco^{QF2Red}* allele, and/or a 367 bp amplicon corresponding to the wild-type allele. Heterozygotes had both wild-type and transgenic PCR bands.

Genotyping *QUAS-mCD8:GFP*

QUAS-mCD8:GFP-11F4 was genotyped using conventional PCR. The PCR reaction used the forward primer: 5′-TCCAGCCGATAGGAACAATC-3′ and reverse primer: 5′-CAAATCCGAATTTCCCGTAA-3′. This resulted in a single 5797 bp amplicon for homozygotes and a 444 bp for the wild-type allele. Heterozygotes typically only had the wild-type PCR band.

Genotyping *QUAS-CaMPARI2-F2*

QUAS-CaMPARI2-F2 was genotyped using a multi-primer PCR assay with the forward primer: 5′-GTTTGACCAAATGCCGTTTC-3′; and two standard reverse primers: 5′-GTCGATAGGCGCGTAGTGTA-3′ and 5′-CACCACTTTTGAAGCGTTGA-3′. Each of the reverse primers is used at half the normal concentration. This results in a single 645 bp amplicon in homozygous mosquitoes, a single 874 bp amplicon in wild-type mosquitoes; and two amplicons, one at 645 bp and one at 874 bp in heterozygous mosquitoes.

Transgenic Stock Maintenance and Composite Genotypes

Gr1^{QF2Red}, *Gr1*^{QF2}, *IR8a*^{QF2Red} and *IR8a*^{QF2} driver lines were maintained as homozygous stocks. *orcoQ*^{F2Red} was maintained as a heterozygous stock by outcrossing to LVPib12 each generation. *orco*^{QF2} was maintained as a heterozygous stock by outcrossing to either *LVPib12* or *QUAS-mCD8::GFP* each generation and screening for GFP fluorescence in the olfactory tissues of the progeny. *15xQUAS-mCD8::GFP* and *15xQUAS-CaMPARI2* responder lines were maintained as homozygous stocks. The *exu-Cre* line was maintained as a heterozygous stock by outcrossing to *LVPib12* each generation. Stock and composite genotypes used in each figure panel are detailed in Table S4. Cytogenetic locations of all transgenes generated in this study are detailed in Figure S10. Cytogenetic locations of all transgenes generated in this study are detailed in Figure S11.

Immunohistochemistry

Immunostaining of female *A. aegypti* brains was performed as previously described (*17*), with minor modifications. Briefly, severed mosquito heads were fixed in 4% paraformaldehyde (Milonig's buffer, pH 7.2) for three hours and brains were carefully dissociated from the head capsule, pigmented ommatidia and air sacks. Dissected brains were then subjected to three 20 min washes at room temperature in PBST (0.1M PBS with 0.25% Triton-X 100), and allowed to incubate overnight in a blocking solution consisting of 2% normal goat serum (NGS) and 4% Triton-X 100 in 0.1M PBS at 4°C. Brains were then washed three times for 20 min each in PBST and incubated for three days at 4°C in a primary antibody solution containing mouse anti-BRP (DSHB, nc82-s, AB_2314866, 1:50 v/v) targeting the pre-synaptic active zone protein *Bruchpilot* (*41*) and rabbit anti-GFP (Invitrogen, A-6455, 1:100 v/v) targeting *mCD8::GFP*. Brains were then washed three times for 20 min each in PBST and incubated for 3 days at 4°C in a secondary antibody solution consisting of goat anti-mouse Cy3 (Jackson ImmunoResearch, AB_2338680, 1:200 v/v) and goat anti-rabbit Alexa Fluor 488 (Invitrogen, A-11008, 1: 200 v/v). All primary and secondary antibody dilutions were prepared in PBST with 2% v/v NGS. Brains were finally washed three times for 20 min each in PBST at room temperature and mounted in 20 ul of Slow-Fade Gold Antifade Mountant (Invitrogen, S36936) on glass slides with coverslip bridges (Number 2-170 µm).

Immunohistochemistry Image Acquisition Settings

Brain immunostaining images were acquired on a single-point laser scanning Carl-Zeiss LSM 780 confocal microscope. To capture images of the entire adult brain, a 10X objective lens (0.3 NA, Plan-Apochromat) was used. Excitation of Cy3 signal was achieved with a 561 nm solid-state

675 laser line at 0.05 % laser power, and GaAsP detector gain set to 825; while a 488 nm laser line
676 was used to excite Alexa Fluor 488 (20% laser power, detector gain at 825). We additionally
677 acquired images with a 20X objective lens (0.8 NA, Plan-Apochromat) to perform 3D
678 reconstructions of the antennal lobes. For these the power of the 488 nm laser line was adjusted
679 to 5%. For each antennal lobe, 60 z-slices with a z-step size of 1 µm and a 1024 X 1024-pixel
680 resolution were acquired.
681
682 **Antennal lobe reconstructions**
683 3D morphological reconstructions of left antennal lobes were performed as previously described
684 (*17*). Briefly, confocal images were imported in *.lsm format into Amira (FEI Houston Inc) and then
685 segmented by highlighting all pixels across a z-stack occupied by individual glomeruli. The nc82
686 channel was used for manual segmentation of individual glomeruli. The *GFP* channel was then
687 used to identify *orco*, *IR8a* and *Gr1*-positive glomeruli. To name glomeruli we identified landmark
688 glomeruli in each antennal lobe sample and using a systematic antennal lobe reference key (*17*)
689 we then designated names to all *GFP* labeled glomeruli based on their spatial positions relative
690 to the landmarks. 3D and 2D antennal lobe models were generated by surface rendering.
691 Glomerular volumes were obtained (μm^3) from the left antennal lobe of five replicate brains using
692 the nc82 channel.
693
694 **Imaging of Peripheral Olfactory Appendages**
695 Live antenna, palp and proboscis tissue were dissected in 0.1M PBS and immediately mounted
696 in Slow-Fade Gold Antifade Mountant (Invitrogen, S36936). Images were acquired on a Carl-
697 Zeiss LSM 780 confocal microscope within 1 hour of dissection. To excite the *GFP* signal, the
698 488 nm laser line was used at 5% laser power. An additional DIC channel was used to visualize
699 gross morphology of the peripheral tissue. Images of the antennae were acquired with a 20X
700 objective lens (0.8 NA, Plan-Apochromat), while images of the palp and labella of the proboscis
701 were acquired with a 40X (1.3 NA, Plan-Apochromat) oil immersion objective.
702
703 **Live Mosquito Preparation for *CaMPARI2* Photoconversion**
704 To prepare mosquitoes for *CaMPARI2* photoconversion (*47*), mosquitoes were cold anesthetized
705 and tethered to an imaging chamber. To do this, the thorax of a female mosquito was first affixed
706 to the ventral surface of a 35mm petri dish lid (Eppendorf, 0030700112) using UV-curing adhesive
707 (Bondic) immediately proximal to a 15mm diameter circular hole made in the lid center. Two
708 additional drops of adhesive were applied to the ommatidia on extremities of the mosquito head,

to prevent head movement. A small piece of clear tape (Duck EZ Start, Heavy Duty Packaging Tape) was then affixed over the center hole such that the dorsal surface of the mosquito head could be gently affixed to the ventral adhesive tape surface. An excised section of plastic coverslip (5mm x 3mm) was then affixed to the tape and used to shield the antennae from the adhesive tape surface and suspend these sensory appendages in the air.

The imaging chamber with head fixed mosquito was then inverted and a rectangular incision window approximately 400 µm X 200 µm was cut through the tape window where the dorsal head cuticle and ommatidia were affixed. The wide boundary of the incision was typically made immediately adjacent to the first antennal subsegment along the lateral-medial brain axis, while the short boundary of the incision extended along the dorsal-ventral brain axis. To create this window, segments of ommatidia and bridge cuticle between the left and right eyes were gently incised and removed using a surgical stab knife (Surgical Specialties Corporation, Sharpoint, Part # 1038016) to reveal the underlying antennal lobes. The exposed antennal lobes were then immediately immersed in an *A. aegypti* Ringer's solution (*59*) composed of 150 mM NaCl, 3.4 mM KCl, 5mM glucose, 1.8 mM $NaHCO_3$, 1 mM $MgCl_2$, 25mM HEPES and 1.7 mM $CaCl_2$; pH 7.1. Mosquitoes were allowed to recover for a period of 15 min from cold anesthesia and surgery in a humidified chamber at room temperature prior to imaging.

CaMPARI2 Photoconversion

For *CaMPARI2* photoconversion, the tethered preparation was then placed under a 20X water dipping objective (Olympus XLUMPLFLN20XW, 1.0 NA) ensuring that the antennal lobes expressing basal green *CaMPARI2* signal were in focus. Each preparation was then exposed to a combined photoconversion-odor stimulation regime consisting of repetitive duty cycles of four 500 ms pulses of 405nm light from an LED driver (Thorlabs, DC4104, 1000mA current setting) synchronized with a 1 s odorant pulse as outlined in Fosque et al. 2015 (*48*), for 75 cycles with a total protocol duration of approximately 41 minutes.

Odorant Delivery

Pulses of odorants were delivered using a custom olfactometer device (Lundström et al 2010) with solenoid valves regulating delivery of odor stimuli from chambers equipped with pressure-sensitive check valves (Smart Products USA, Inc.). 3mL of control (dH2O) or treatment (L-(+)-lactic acid solution, Sigma Aldrich, 27714) odors were placed into dedicated and sealed odor delivery vials. During 'odor onset', synthetic air (Airgas, AI UZ300) at a flow rate of 1ml/s was

743 passed through these holding chambers to carry headspace odors via Teflon tubing into a carrier
744 airstream of humified synthetic air that was directed at the olfactory appendages of the mosquito
745 using a plastic pipette. During *CaMPARI2* photoconversion assays, the tethered mosquito
746 preparation always received a constant amount of airflow (5ml/s) during odor onset/offset from
747 the stimulus pipette via solenoid valves simultaneously switching or combining humidified
748 synthetic air, 5% CO_2 (Airgas, CD USP50) and L-(+)-lactic acid headspace as required for
749 different odor treatments. In trials involving CO_2, a 1ml/s stream of 5% CO_2 was diluted 1:5 into
750 the carrier airstream for a final concentration at the specimen of 1%.
751
752 ***CaMPARI2* Sample Processing**
753 Following photoconversion, the mosquito was gently untethered from the imaging chamber and
754 the head severed and fixed in Milonig's buffer for 20 minutes. The brain was then dissected out
755 in calcium-free Ringer's solution composed of 150 mM NaCl, 3.4 mM KCl, 5 mM glucose, 1.8 mM
756 $NaHCO_3$, 1 mM $MgCl_2$, 25 mM HEPES and 10 mM EGTA. To stain glomerular boundaries, we
757 then incubated each brain in Alexa Fluor 647 Phalloidin (Invitrogen, A22287) prepared in calcium-
758 free Ringer's solution (1:40 v/v dilution) for 30 min. To prepare Alexa Fluor 647 phalloidin for use
759 in imaging, first, a 400X DMSO stock solution was prepared according to the manufacturer's
760 instructions by dissolving the fluorophore in 150 ul of DMSO. 1 ul of this DMSO stock was diluted
761 in 399 ul calcium-free Ringer's solution to yield a 1X stock. This stock was then further diluted to
762 a final concentration 1:40 in calcium-free Ringer's solution for staining. Brains were transferred
763 directly from this solution into 20 ul of Slow-Fade Gold Antifade Mountant (Invitrogen, S36936) on
764 glass slides with coverslip bridges (Number 2- 170 μm) for *CaMPARI2* and phalloidin imaging.
765
766 ***CaMPARI2* Image Acquisition Settings**
767 Antennal lobes from *CaMPARI2* photoconversion assays were imaged with a 63X (1.4 NA) oil-
768 immersion objective on a Zeiss 880, Airyscan FAST super-resolution single point scanning
769 microscope. Excitation of red *CaMPARI2* signal was achieved with a 561 nm solid-state laser line
770 at 14 % laser power. Green *CaMPARI2* was excited with a 488 nm argon laser line at 10% laser
771 power. To visualize glomerular boundaries, a 633 nm diode laser was used to excite the Alexa-
772 647 phalloidin fluorophore at 40% laser power. Master detector gain was set to a value of 800.
773 We captured 0.987 μm z-slices of 1572 X 1572-pixel resolution in the FAST mode. Raw images
774 were further processed by applying the Airyscan method with 'auto' processing strength.
775
776 ***CaMPARI2* Image Analysis**

Image analysis was carried out in Fiji (http://imagej.net/Fiji) and images were imported into the program in the *.lsm format. We first applied a median filter (radius= 2 pixels) to remove noise and then a rolling ball subtraction (rolling ball radius =80 pixels), to correct for non-uniformity of background intensities. We analyzed *CaMPARI2* photoconversion in the left antennal lobe of all samples due the well-defined spatial arrangement and conspicuous boundaries of *IR8a*-positive glomeruli in this lobe with phalloidin straining. ROIs were defined by manually segmenting glomeruli using the free hand selection tool. For *IR8a* glomeruli, we analyzed photoconversion ratios for 12/15 *IR8a*-positive glomeruli that could be reliably identified across all AL samples. These included: VC5, VC6, PL1-PL6, PM4, PC4, CD2 and CD3. The integrated density (mean grey value X area) for all z- slices of the ROI, which included all representative slices of a target glomerulus, was calculated in the green (488 nm) and red (560 nm) imaging channels. The final measure of photoconversion, the red to green ratio (R/G), was calculated as:

$$R/G = \text{Average integrated density of ROI}^{(RED)} / \text{Average integrated density of ROI}^{(GREEN)}$$

Glomeruli were named by co-localizing green and red *CaMPARI2* signal to individual glomeruli evident in the Alex-Fluor 647 phalloidin channel and defining their spatial orientation relative to landmark and flanking glomeruli using our 2D *CaMPARI2*-phalloidin antennal lobe reference map.

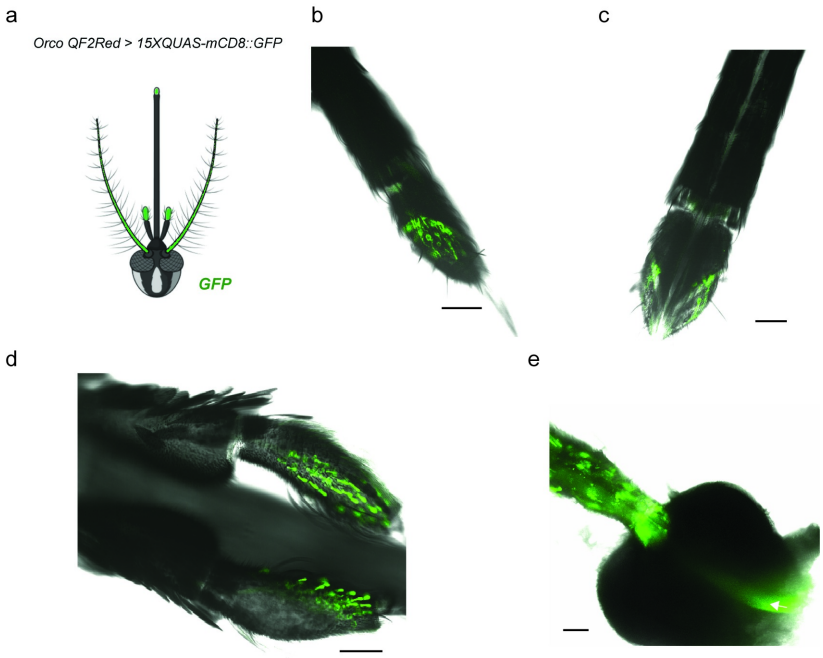

Figure S1. Additional peripheral innervation patterns of *orco* (+) olfactory sensory neurons on *A. aegypti* sensory appendages. (a) Schematic of the mosquito head showing the gross expression pattern from *orco*^{QF2Red} > *15XQUAS-mCD8::GFP* females in peripheral olfactory tissue. **(b-c)** In addition to the third antennal segment shown in Figure 1, strong GFP expression from dorsal and ventral perspectives of the labella of the proboscis. Axonal projections of these neurons extend into the shaft of the proboscis. **(d)** *orco* expression was also strongly evident within capitate peg sensilla on the ventral surface of the maxillary palp. **(e)** Maximum intensity projection of a female pedicel at 40X magnification. No *orco* expression was noted in the scolopidia of the pedicel while the antennal nerve was observed to transect the pedicel Scale bar: 50 μm.

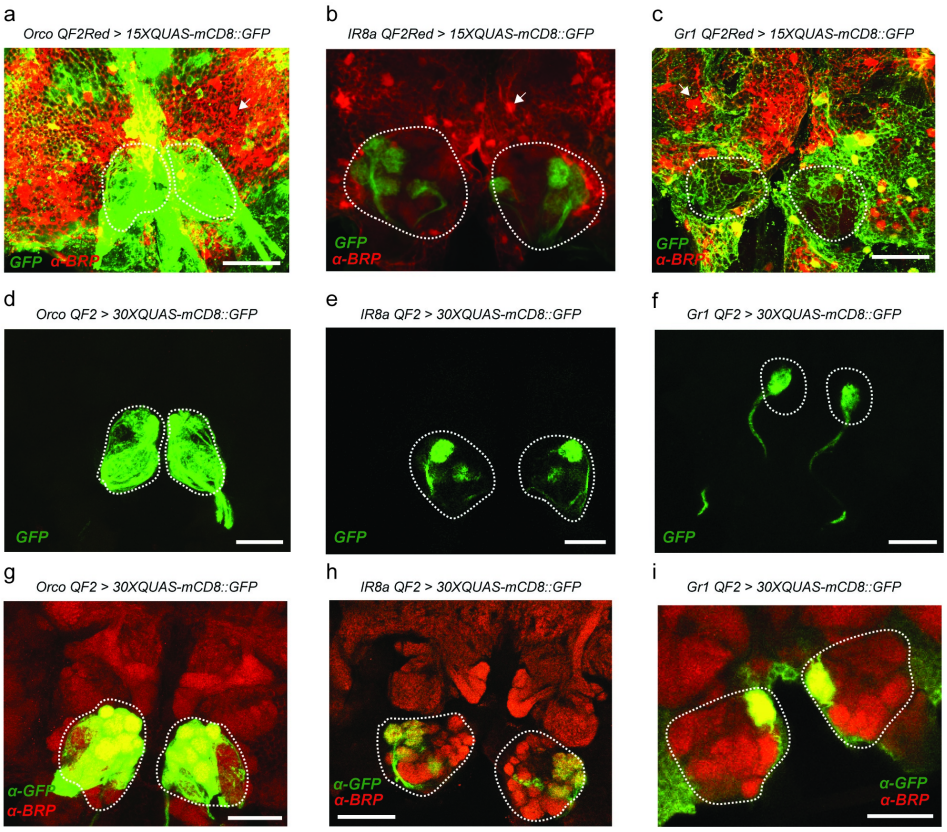

Figure S2. Promiscuous *QF2/QUAS* driven fluorescence in the *A. aegypti* brain and *Cre-LoxP* mediated excision of *3xP3* marker cassettes. The transgenic *QF2*^{Red} driver lines described in this study carried a floxed *3xP3-DsRed2* cassette to mark successful transgenesis. However, upon close examination of the central brain we noted that this marker cassette was not only expressed in the optic lobes, but was also strongly expressed in hexagonal cells ensheathing the central brain which are putatively glia (arrows). In crosses involving the *orco*^{QF2Red} and *Gr1*^{QF2Red} driver lines, we also noted conspicuous green expression in these same locations suggesting the *3xP3* promoter was influencing the expression pattern of the integrated *T2A-QF2* transgene at these loci. **(a-c)** Anterior view of adult female mosquito brains at 20X magnification. *3xP3* expression occludes the antennal lobes and other neuropil, in each of the three driver lines, posing a significant challenge for confocal or two-photon imaging. Genetic excision of this marker from the *QF2* driver lines alone markedly improved our ability to clearly view the antennal lobes in both unstained **(d-f)** and immunostained brain preparations **(g-i)**. Scale bar: 50 μm.

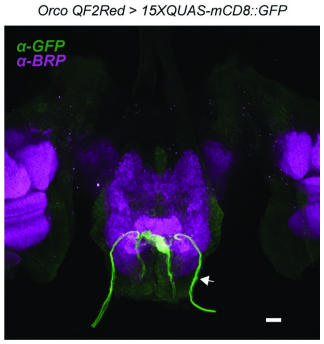

Figure S3. SEZ innervation of *orco* (+) neurons. Posterior view of the brain of an adult female *orco*^{QF2} > *30XQUAS-mCD8::GFP* mosquito. *orco* (+) neurons from the labella project via the labial nerve (arrow) and terminate in the gustatory center of the mosquito brain, the suboesophageal zone (SEZ). In *Anopheles gambiae*, these terminal neuropil clusters were well separated and named SEZ glomeruli (Riabinina et al., 2016). In *Aedes aegypti* the boundaries of these clusters overlap and appear to be smaller in size. Scale bar: 20 μm.

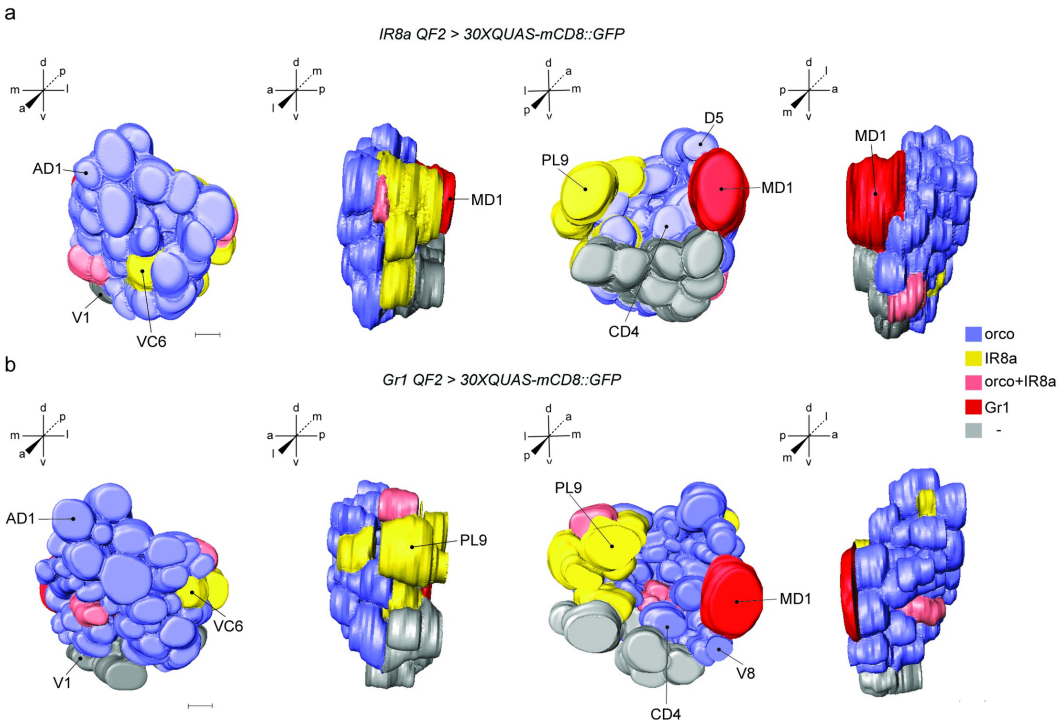

Figure S4. Three-dimensional models of the female antennal lobe from *Ir8a* and *Gr1* driver lines. 3D reconstructed models of the left antennal lobe from adult female *Aedes aegypti* from **(a)** *IR8a*^{QF2} > *30XQUAS-mCD8::GFP* and **(b)** *Gr1*^{QF2} > *30XQUAS-mCD8::GFP* genotypes are illustrated. 3D models are arranged (left to right) in the anterior, lateral, posterior and medial orientations. *orco* (+) glomeruli, *IR8a* (+) glomeruli, *orco* (+) / *IR8a* (+) glomeruli, and the *Gr1* (+) (MD1) glomerulus are colored blue, yellow, orange and red respectively. Eight landmark glomeruli including AD1 and VC6 on the anterior surface, and MD1, V1, V8, PL9, CD4 and D5 on the posterior AL surface are labelled. Scale bar: 10 µm. These models are shown in 2D format in Figure S6 and S7.

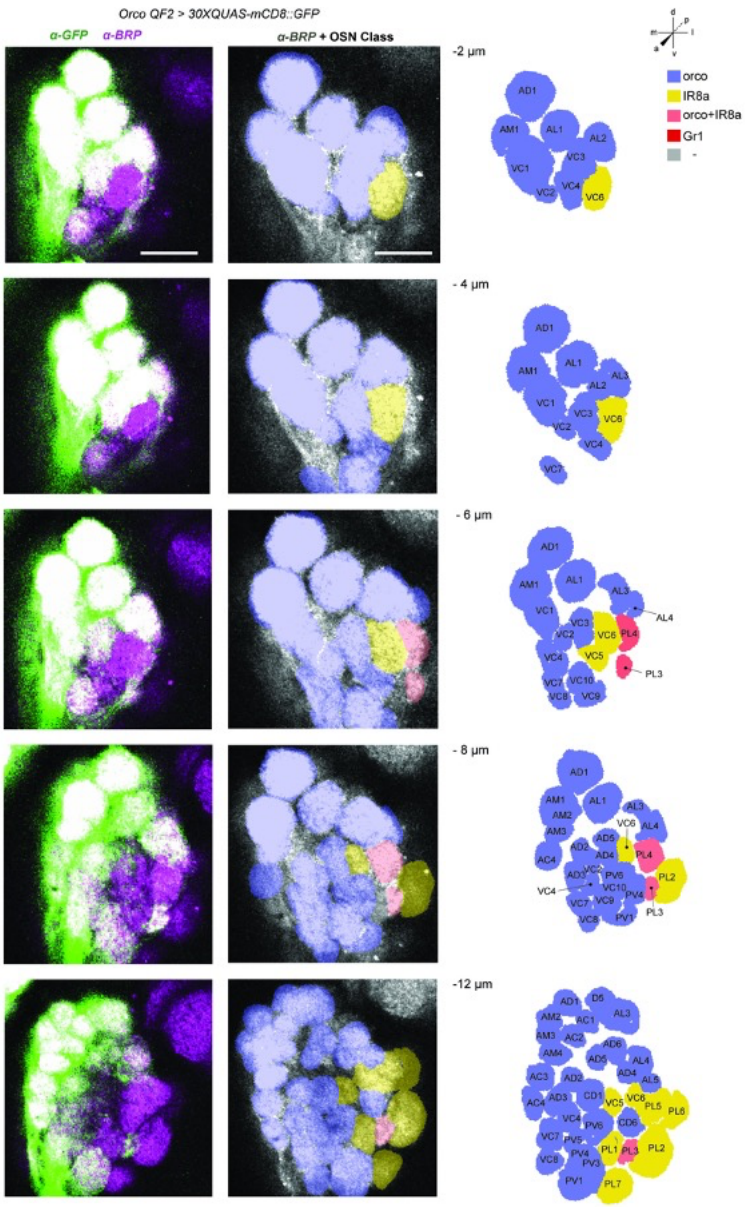

Figure S5. *orco* Receptor to Glomerulus 2D Map.

Representative confocal stack from the left antennal lobe of an adult female *orco*^{QF2} > *30XQUAS-mCD8::GFP* mosquito. The left panels show the antennal lobe at 20X magnification, with the GFP signal from *orco* neurons in green and the neuropil stained with BRP in magenta, to visualize glomerular boundaries. The middle panels show the BRP stained glomeruli overlayed with blue (*orco*+), yellow (*Ir8a*+), orange (putatively *orco*+ and *Ir8a*+), red (*Gr1*+), and grey colors (unknown chemosensory identity). The right panels show detailed spatial maps of all antennal glomeruli, glomeruli are color coded according to chemoreceptor class. 10 representative focal planes from a total of 60 z-slices are shown on this map. *orco* neurons innervate 60 glomeruli. These included all the anterior glomerular groups namely, the Antero-Dorsal (AD), Antero-Lateral (AL), Antero-Medial (AM), Antero-Central (AC) and the Ventro-Central (VC) groups. The posterior groups innervated by *orco* (+) neurons include the Postero-Medial (PM), Postero-Central (PC), Postero-Lateral (PL), Centro-Dorsal (CD), Postero-Ventral (PV), Dorsal (D) and Medio-Dorsal (MD) groups. A total of 49 spatially invariant glomeruli depicted in blue are shown in this 2D map. Scale bar: 10 µm.

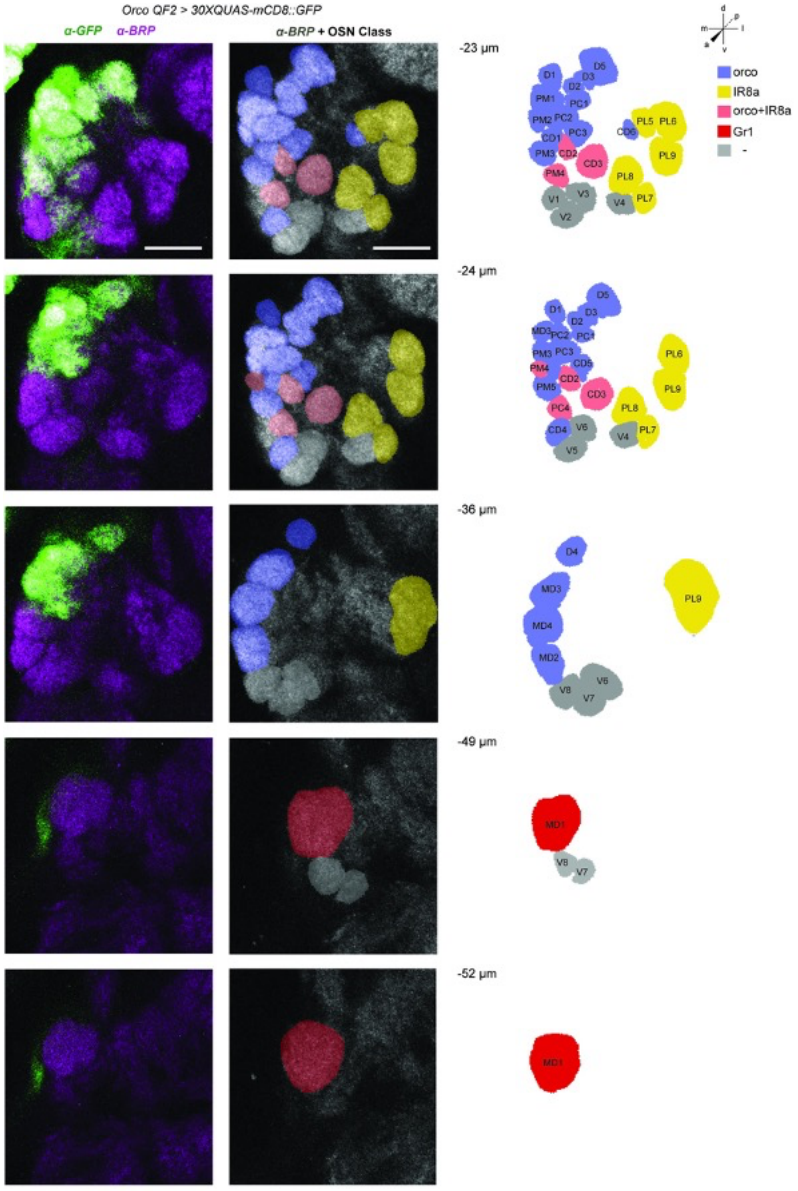

Figure S5 (continued). *orco* Receptor to Glomerulus 2D Map.

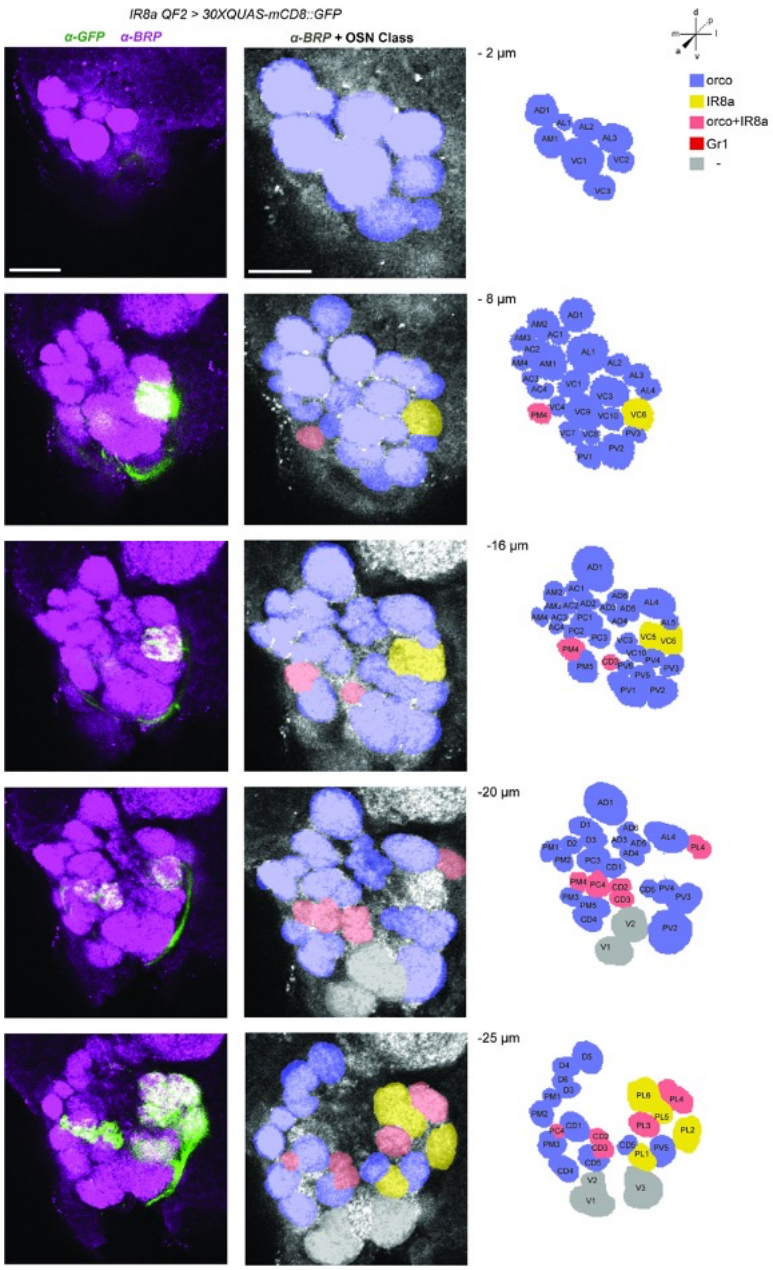

Figure S6. *IR8a* Receptor to Glomerulus 2D Map

Representative confocal stack from the left antennal lobe of an adult female *Ir8a*^{QF2} > *30XQUAS-mCD8::GFP* mosquito. 7 representative focal planes from a total of 44 z-stacks are shown on this map. *Ir8a* neurons innervate 15 total glomeruli: 2 glomeruli of the anteriorly positioned VC group (VC5 and VC6), 9 glomeruli of the PL group (PL1-9), 2 CD glomeruli (CD2 and CD3), 1 PC group glomerulus (PC4) and 1 PM group glomerulus (PM4). Glomeruli CD2, CD3, PL3, PL4, PC4, PM4 are putatively co-innervated by *orco* (+) and *IR8a* (+) neurons. *IR8a* (+) glomeruli are spatially invariant. Scale bar: 10 µm.

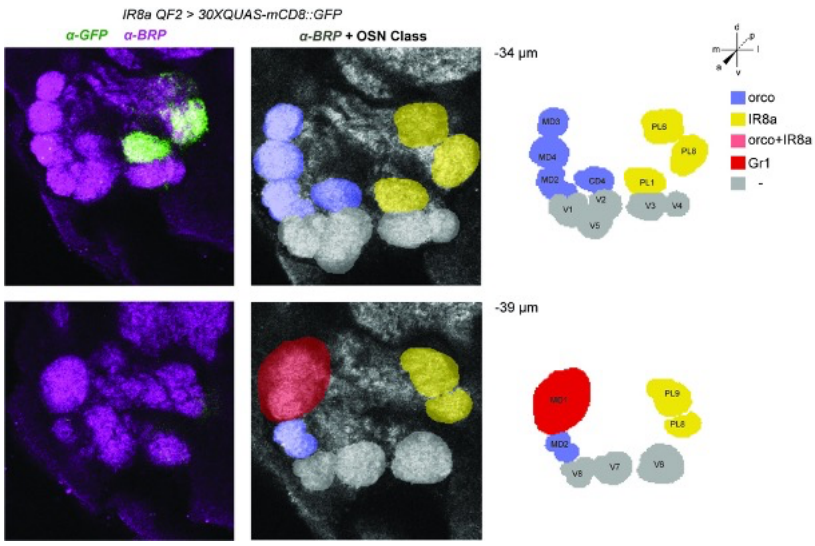

Figure S6 (continued). *IR8a* Receptor to Glomerulus 2D Map.

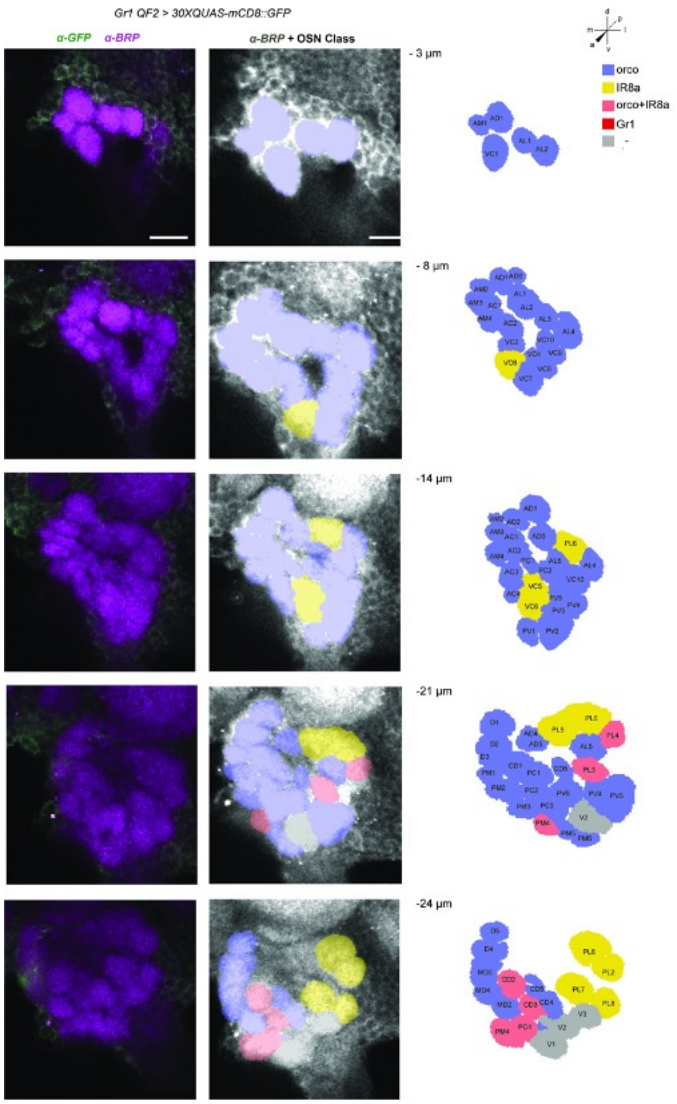

Figure S7. *Gr1* Receptor to Glomerulus 2D Map

Representative confocal stack from the left antennal lobe of an adult female *Gr1*^{QF2} > *30XQUAS-mCD8::GFP* mosquito. 7 representative focal planes from a total of 50 z-stacks are shown on this map. Scale bar: 10 µm. *Gr1* neurons project to the spatially invariant MD1 glomerulus. No innervation *of Orco, Ir8a or GR1* neurons was observed in the Ventral (V) group. Scale bar: 10 µm.

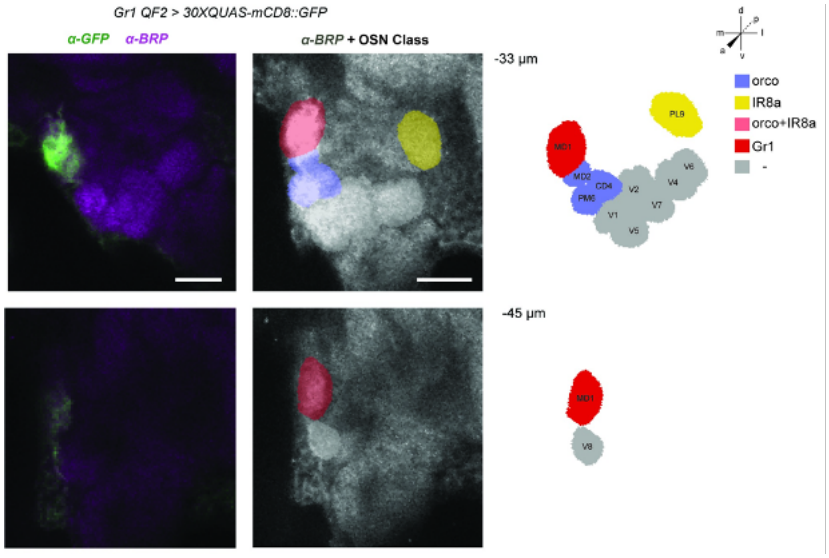

885
886
887
888 **Figure S7 (continued). *Gr1* Receptor to Glomerulus 2D Map.**
889

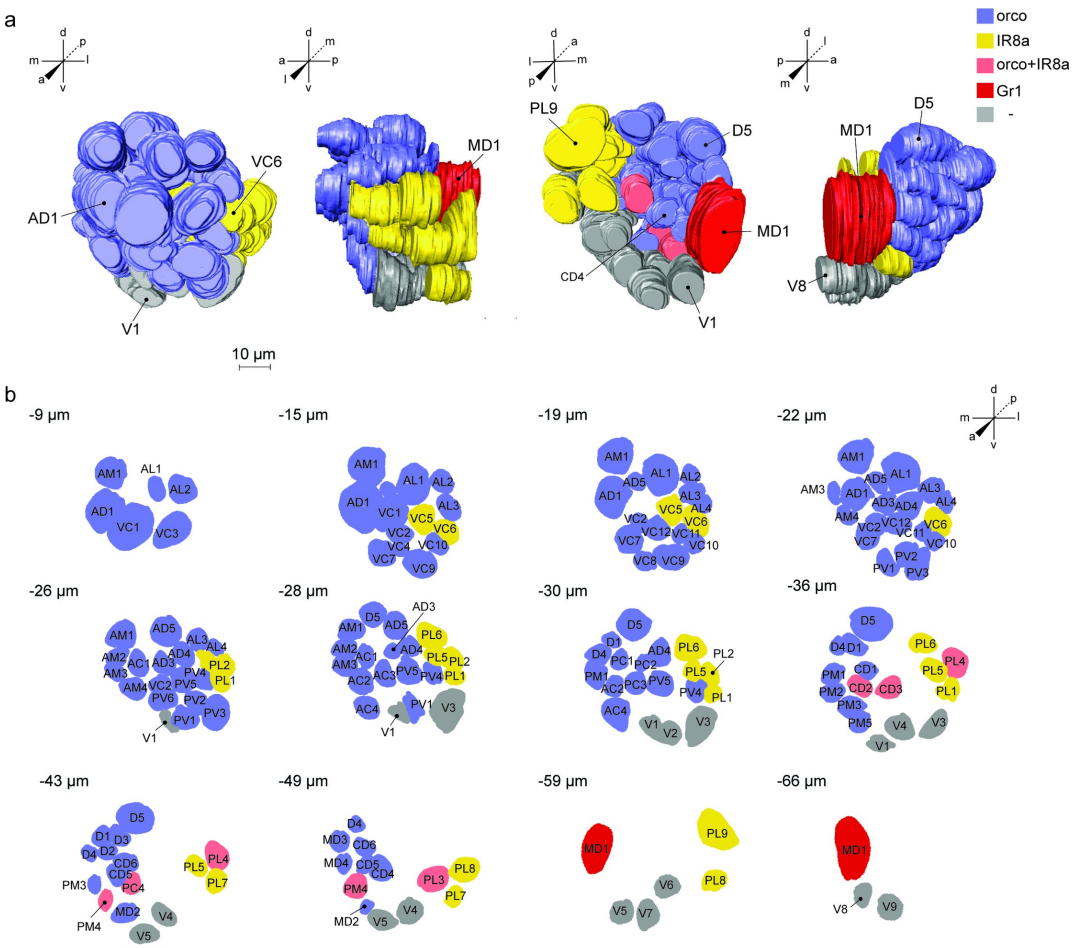

Figure S8: Phalloidin-stained LVPib12 female antennal lobe model used as a reference map for CaMPARI2 activity dependent labeling.

(a) 3D model generated from a female LVib12 left antennal lobe stained with Alexa Fluor 647-phalloidin and imaged at 63X magnification from anterior, lateral, posterior and medial perspectives. Glomeruli are color coded according to chemoreceptor class. Landmark glomeruli are highlighted on the model. **(b)** 2D reference map for CaMPARI labelling. Scale bar: 10 µm.

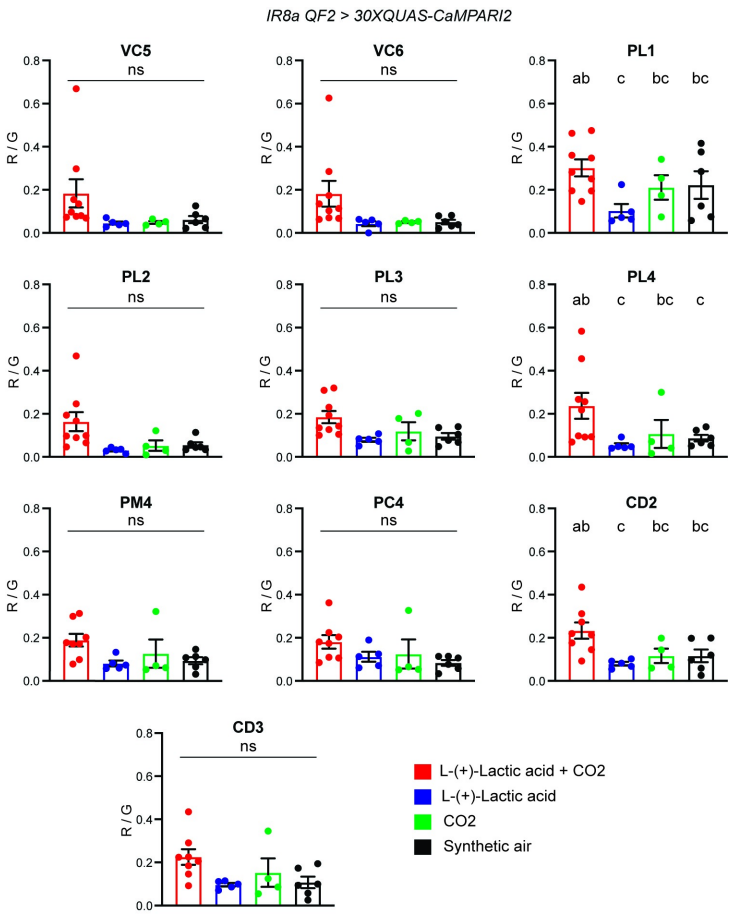

Figure S9: CaMPARI2 Photoconversion In Supplemental *IR8a* (+) Glomeruli Screened in Response to Unitary and Binary Blends of L-(+)-lactic acid and CO_2.

Comparisons of CaMPARI2 photoconversion revealed no significant differences in glomerular photoconversion in VC5, VC6, PL2, PL3, PM4 and CD3 glomeruli with any of the four odorant stimuli (L-(+)-lactic acid + CO2; L-(+)-lactic acid alone, CO2 alone; and synthetic air). Of the remaining glomeruli, PL5 and PL6 reported in the main text, and PL4 and CD2 glomeruli reported here exhibited photoconversion ratios where the 'L-(+)-lactic acid + CO2' stimulus had mean R/G values that were significantly elevated relative to all or some of the other stimuli. For example, the PL4 glomerulus had mean photoconversion values for 'L-(+)-lactic acid +CO2 vs Synthetic Air', $P = 0.0320$; and 'L-(+)-lactic acid + CO2 vs L-(+)-lactic acid', $P = 0.0094$; that were significantly different. For the CD2 glomerulus, differences between mean R/G values for 'L-(+)-lactic acid + CO2 vs L-(+)-lactic acid' also reached statistical significance ($P = 0.0481$). Tukey's Multiple Comparison Test, n = 4-9 brains per stimulus, mean R/G values +/- s.e.m. plotted.

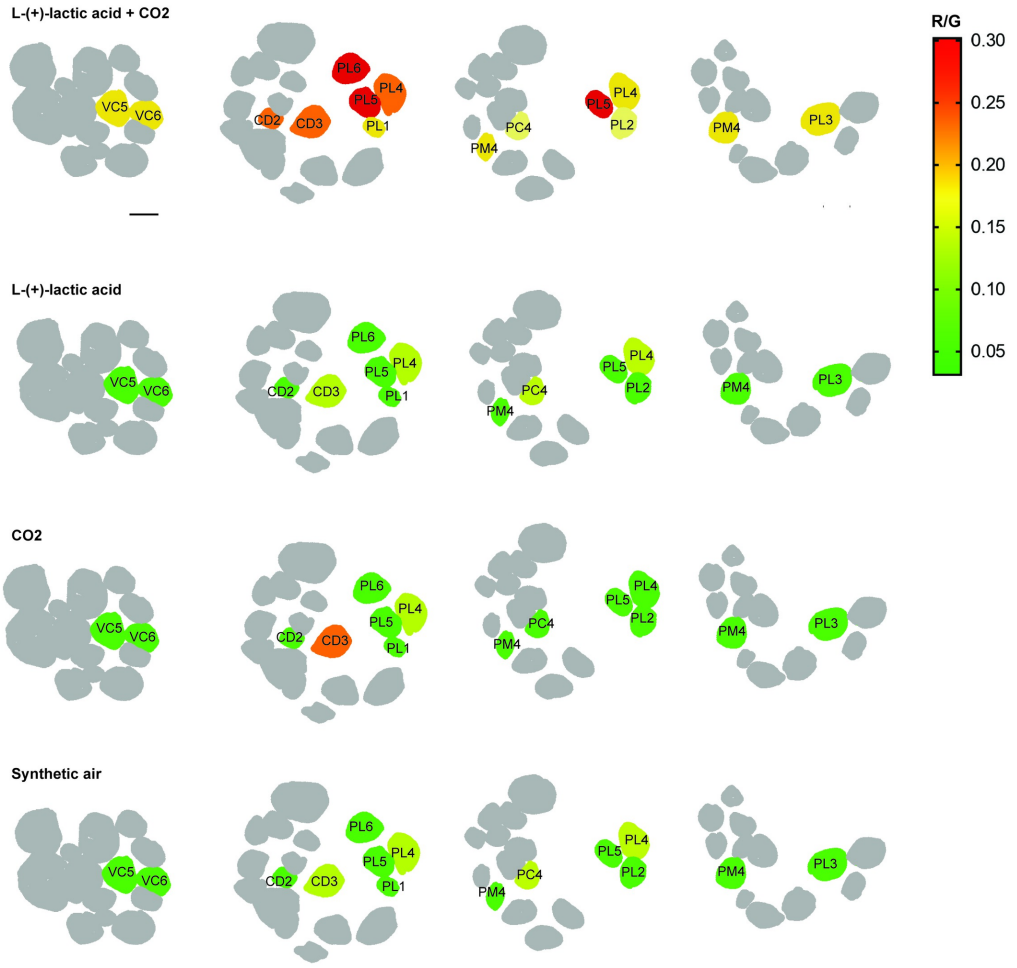

Figure S10: Mean Red/Green CaMPARI2 photoconversion values of *IR8a* (+) glomeruli plotted as a heat map on the phalloidin reference atlas. Average photoconversion (R/G) values for L(+)-lactic acid + 1% CO_2; L(+)-lactic acid alone, CO_2 alone; and a synthetic air control are shown. Scale bar: 10 µm. In total 12 out of 15 total IR8a (+) were included in this screen, with three IR8a (+) glomeruli (PL7, PL8 and PL9) not included because they were not clearly identified across all brain samples.

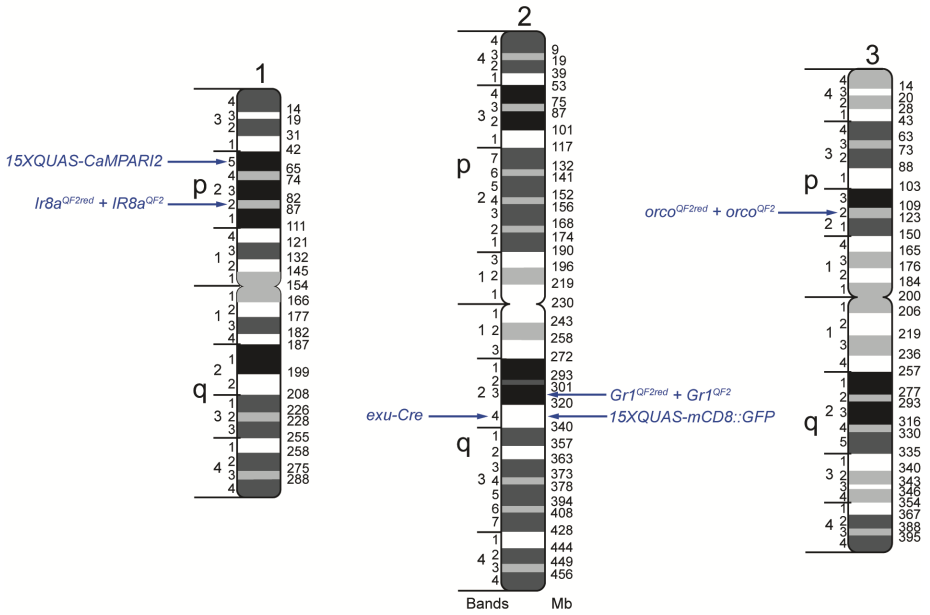

Figure S11. Physical Positions of Transgenes on *Aedes aegypti* Chromosome 1, 2 and 3. *T2A-QF2* in-frame fusion cassettes were precisely inserted at *orco* (AAEL005776), *IR8a* (AAEL002922) and *Gr1* (AAEL002380) loci via CRISPR-Cas9 homologous recombination, while exu-Cre, *15XQUAS-mCD8::GFP* and *15XQUAS-CaMPARI2*, were inserted into the mosquito genome using *Mos1 mariner* transposition with integration sites mapped using Splinkerette PCR.

Table S1. CRISPR Target Sites and Locations

Gene	**Identifier**	**Chromosome**	**Band**	**CRISPR target site** (with N**GG**)	**Cut Site**
orco	AAEL005776	3	3p22	CCATCAAGGCTTGGTACCCG T**GG**	Exon 3
IR8a	AAEL002922	1	1p22	TCCAACGCGAAAGTACCGCT T**GG**	Exon 3
Gr1	AAEL002380	2	2q23	TGACCATGAGGTACTTATAC T**GG**	Exon 3

Table S2. Homology Arms for *T2A-QF2* Donor Constructs

Gene region	**Homology Arm Size (bp)**	**Homology Arm Primers with In-Fusion Adapters (underlined)**
Gr1 Left Arm	1003	5'-TATAACCCGCCTCGGTTATTCCGTTTGTTTTCAATTTTCCGCG-3' 5'-TGCCGCGGCCCTCTCCGCTTCCCTGGTAGTCGGTCCACATGT-3'
Gr1 Right Arm	884	5'-TGACAGATCTGCGCGTAAGTACCTCATGGTCACCGGA-3' 5'-GATATCGATCGCGCGACCGTTTGGAGGTTGAATTG-3'
Orco Left Arm	2624	5'-TATAACCCGCCTCGGTGCAAGTGGATCATTTGTCG-3' 5'-TGCCGCGGCCCTCTCCGCTTCCGTACCAAGCCTTGATGGGC-3'
Orco Right Arm	1329	5'-TGACAGATCTGCGCGCCGTGGGATGCAATGAG-3' 5'-GATATCGATCGCGCGGTGCAATTGTGCCATTTTGA-3'
IR8a Left Arm	2159	5'-TATAACCCGCCTCGGCAAAGTATAATTTCGCCCCCTCC-3' 5'-TGCCGCGGCCCTCTCCGCTTCCCTTGGTCGGTTTGATCTTCTG-3'
IR8a Right Arm	1964	5'-TGACAGATCTGCGCGGGTACTTTCGCGTTGGAACTA-3' 5'-GATATCGATCGCGCGCTCTATGGCAGCCAAGATATTGG-3'

943 **Table S3. Template Materials for Constructs**

Plasmid	Element	Source		Addgene #
pBlackbird				
	3xP3-ECFP-SV40	pBAC-ECFP-15xQUAS-TATA-SV40		104875
	T2A-QF2-hsp70-loxP	pHACK-QF2		80274
	3xP3 promoter	pBAC-ECFP-15xQUAS-TATA-SV40		104875
	DsRed2-SV40	pMOS-3xP3-DsRed		n/a
All reporter constructs				
	Mos1 and ECFP marker	pMos{3xP3-ECFPaf}		n/a
	15xQUAS promoter	pBAC-ECFP-15xQUAS-TATA-SV40		104875
	Syn21 enhancer	pJFRC81-10XUAS-IVS-Syn21-GFP-p10		36432
	p10 terminator	pJFRC81-10XUAS-IVS-Syn21-GFP-p10		36432
pMos-ECFP-QUAS-mCD8::GFP				
	mCD8:GFP	pQUASp-mCD8::GFP		46163
pMos-loxP-ECFP-loxP-QUAS-CaMPARI2				
	CaMPARI2	pAAV-hsyn1-CaMPARI2	gift of E. Schreiter	
pMos-EYFP-exu-Cre				
	Mos1	pMOS-3xP3-dsRed		n/a
	Polyubiquitin promoter	pSL1180-HR-PUbECFP		47917
	EYFP	pBAC-YFP-QF2-hsp70	gift of C. Potter	
	exuperantia promoter	*AAEL010097-Cas9* mosquitoes	gift of O. Akbari	
	Cre recombinase	pENTR L1-vas2-Cre-L4		62301
	p10 terminator	pJFRC81-10XUAS-IVS-Syn21-GFP-p10		36432

944
945

946 **Table S4. Complete Genotypes of *Aedes aegypti* Stocks and Composite Genotypes**
947

Identifier	ABBREVIATED GENOTYPE		FULL GENOTYPE (*Aedes aegypti* chromosome 1; 2; 3) + = wild-type allele
Stock	*LVPib12*	*wild-type*	+/+; +/+; +/+
Stock	*Gr1$^{QF2Red.}$*	*marker = 3xP3-dsRed2, 3xP3-ECFP*	+/+; *Gr1^{QF2Red}* / *Gr1^{QF2Red}*; +/+
Stock	*IR8a^{QF2Red}*	*marker = 3xP3-dsRed2*	*IR8a^{QF2Red}* / *IR8a^{QF2Red}*; +/+; +/+
Stock	*orco$^{QF2Red.}$*	*marker = 3xP3-dsRed2*	+/+; +/+; *orco^{QF2Red}* / +
Stock	*Gr1^{QF2}*	*marker-free*	+/+; *Gr1^{QF2}* / *Gr1^{QF2}*; +/+
Stock	*IR8a^{QF2}*	*marker-free*	*IR8a^{QF2}* / *IR8a^{QF2}*; +/+; +/+
Stock	*orco^{QF2}*	*marker-free*	+/+; +/+; *orco^{QF2}* / +
Stock	*15XQUAS-mCD8::GFP*	*marker = 3xP3-ECFP*	+/+; *15XQUAS-mCD8::GFP* / *15XQUAS-mCD8::GFP*; +/+
Stock	*15XQUAS-CaMPARI2*	*marker = 3xP3-ECFP*	*15XQUAS-CaMPARI2* / *15XQUAS-CaMPARI2*; +/+; +/+
Stock	*exu-Cre*	*marker = PUb-EYFP*	+/+; *exu-Cre* / +; +/+
Composite	*Gr1^{QF2} > 30XQUAS-mCD8::GFP*		+/+; *15XQUAS-mCD8::GFP*, *Gr1^{QF2}* / *15XQUAS-mCD8::GFP*; +/+
Composite	*orco^{QF2} > 30XQUAS-mCD8::GFP*		+/+; *15XQUAS-mCD8::GFP* / *15XQUAS-mCD8::GFP*; *orco^{QF2}* / +
Composite	*IR8a^{QF2} > 30XQUAS-mCD8::GFP*		*IR8a^{QF2}* / +; *15XQUAS-mCD8::GFP* / *15XQUAS-mCD8::GFP*; +/+
Composite	*Gr1^{QF2Red} > 15XQUAS-mCD8::GFP*		+/+; *Gr1^{QF2Red}* / *15XQUAS-mCD8::GFP*; +/+
Composite	*orco^{QF2Red} > 15XQUAS-mCD8::GFP*		+/+; *15XQUAS-mCD8::GFP* / +; *orco^{QF2Red}* / +
Composite	*IR8a^{QF2Red} > 15XQUAS-mCD8::GFP*		*IR8a^{QF2Red}* / +; *15XQUAS-mCD8::GFP* / +; +/+
Composite	*IR8a^{QF2} > 30XQUAS-CaMPARI2*		*IR8a^{QF2}*,*15XQUAS-CaMPARI2* / *15XQUAS-CaMPARI2*; +/+; +/+
Composite	*Gr1^{QF2} > 30XQUAS-CaMPARI2*		*15XQUAS-CaMPARI2* / *15XQUAS-CaMPARI2*; *Gr1^{QF2}* / +; +/+
Composite	*orco^{QF2} > 15XQUAS-CaMPARI2*		*15XQUAS-CaMPARI2* / +; +/+; *orco^{QF2}* / +

948

949

950 **Table S5. Genomic Integration Sites of *Mos1 mariner* transgenes**

Transgene	Chromosome	Band	Insertion Site	Insertion Location
15XQUAS-CaMPARI2	1	1p25	65092968	AAEL026960, Intron
15XQUAS-mCD8::GFP	2	2q24	329084910	Upstream of AAEL021072 lncRNA
exu-Cre	2	2q24	324350134	AAEL013635, Intron

951

952

953

954

955

956